

ORIGINAL PAPER

Open Access



Reassessing the intrusive tempo and magma genesis of the late Variscan Aar batholith: U–Pb geochronology, trace element and initial Hf isotope composition of zircon

Mélissa Ruiz¹, Urs Schaltegger^{1*} , Sean P. Gaynor¹ , Massimo Chiaradia¹ , Jürgen Abrecht², Christian Gisler³, Federico Giovanoli⁴ and Michael Wiederkehr⁵

Abstract

The Variscan orogeny was responsible for the formation of a significant volume of igneous basement throughout present-day Europe. Detailed understanding of these rocks has, however, been obfuscated by significant overprinting during younger geologic events. In order to better understand the formation of this basement, we present U–Pb dates, trace element concentrations and Hf isotope compositions of zircon from 17 intrusions of the Variscan Aar batholith, located in the Aar Massif, Central Alps, Switzerland. Laser ablation inductively coupled plasma mass spectrometry (LA-ICPMS) was used to generate a large set of U–Pb dates, trace element and Hf isotope compositions on untreated zircon, as well as zircon pretreated by chemical abrasion. Furthermore, a subset of samples was also analyzed for high-precision U–Pb geochronology using chemical abrasion, isotope dilution, thermal ionization mass spectrometry (CA-ID-TIMS). The U–Pb dates of both dating techniques are significantly dispersed, indicating that they are influenced by multiple forms of complexity, including inheritance, domains of secondary alteration likely related to Alpine overprint or growth, decay damage related Pb-loss, and potentially protracted magmatic growth. Decay-damage related Pb-loss is likely a subordinate source of age scatter within the data, therefore chemical abrasion pretreatment is not capable of completely mitigating the observed analytical scatter. After rejection of outliers, the remaining data still exhibit excess scatter of several percent among $^{206}\text{Pb}/^{238}\text{U}$ dates in individual samples, however it is possible to interpret reasonable geologic ages from these data. These new U–Pb zircon age interpretations indicate the Aar batholith grew incrementally through four major magmatic pulses, which occurred at approximately 348, 333, 309 and 298 Ma. Based on the trace element and Hf isotope geochemistry, the melt source(s) of the Aar batholith evolved throughout the duration of batholith formation and growth. The transitioning from (i) melting of depleted mantle at 348 Ma during a stage of active continental arc magmatism ($\epsilon\text{Hf} = +12$ to $+10$), (ii) melting of metasomatically enriched lithospheric mantle, possibly contaminated by crust during the 333 Ma pulse ($\epsilon\text{Hf} = -10$ to -3), followed by (iii) an increasing incorporation of a juvenile mantle components during the 309 and 298 Ma pulses ($\epsilon\text{Hf} = -3$ to $+6$). Finally, these new U–Pb ages yield a more detailed understanding of the Variscan Aar batholith by

Editorial handling: Paola Manzotti.

*Correspondence: urs.schaltegger@unige.ch

¹ Département des Sciences de la Terre, Université de Genève, rue des Maraichers 13, 1205 Geneva, Switzerland
Full list of author information is available at the end of the article



© The Author(s) 2022. **Open Access** This article is licensed under a Creative Commons Attribution 4.0 International License, which permits use, sharing, adaptation, distribution and reproduction in any medium or format, as long as you give appropriate credit to the original author(s) and the source, provide a link to the Creative Commons licence, and indicate if changes were made. The images or other third party material in this article are included in the article's Creative Commons licence, unless indicated otherwise in a credit line to the material. If material is not included in the article's Creative Commons licence and your intended use is not permitted by statutory regulation or exceeds the permitted use, you will need to obtain permission directly from the copyright holder. To view a copy of this licence, visit <http://creativecommons.org/licenses/by/4.0/>.

integrating the new detailed mapping of Aar Massif for the Geological Atlas of Switzerland, allowing for more accurate characterization and categorization of variably deformed heterogeneous intrusive bodies.

1 Introduction

The Variscan orogen formed at the end of the Paleozoic, between ca. 370 and 290 Ma, during the subduction of the Saxo-Thuringian ocean and the subsequent collision of Eurasia with Gondwana. Remnants of this orogeny are accessible in Europe through a series of windows (“massifs”) within younger, mostly sedimentary cover (as, e.g., Iberia, French Massif Central, Armorica, Vosges-Black Forest, the Bohemian massif, and Corsica-Sardinia). Late-orogenic processes in the Variscan orogen (between 340 and 290 Ma) are mainly represented by a large volume of migmatites in lower and middle crustal levels and intrusive rocks in the middle to shallow crust. The latter are spatially associated with coeval sedimentary basins, testifying their emplacement within a largely extensional to transtensional context. Recent studies have integrated collisional processes, crustal and mantle melting, magmatism and tectonics into a plate tectonic model in the Massif Central (Vanderhaeghe et al., 2020), the Vosges (Hora et al., 2021; Tabaud et al., 2015), the Bohemian Massif (Janoušek et al., 2000; Schulmann et al., 2014), or in Sardinia (Conte et al., 2017). However, the Variscan basement of the Alps is comparably less well studied, despite that it represents a nearly continuous outcrop of Variscan and pre-Variscan rocks (Ballèvre et al., 2018; Guillot & Ménot, 2009; von Raumer et al., 2013). The late-Variscan magmatism is particularly well exposed in the so-called “external massifs” in the Helvetic realm of the Alpine chain (Argentière, Haut-Dauphiné, Belledonne, Mont Blanc-Aiguilles Rouges, Aar Massif, Gotthard Nappe).

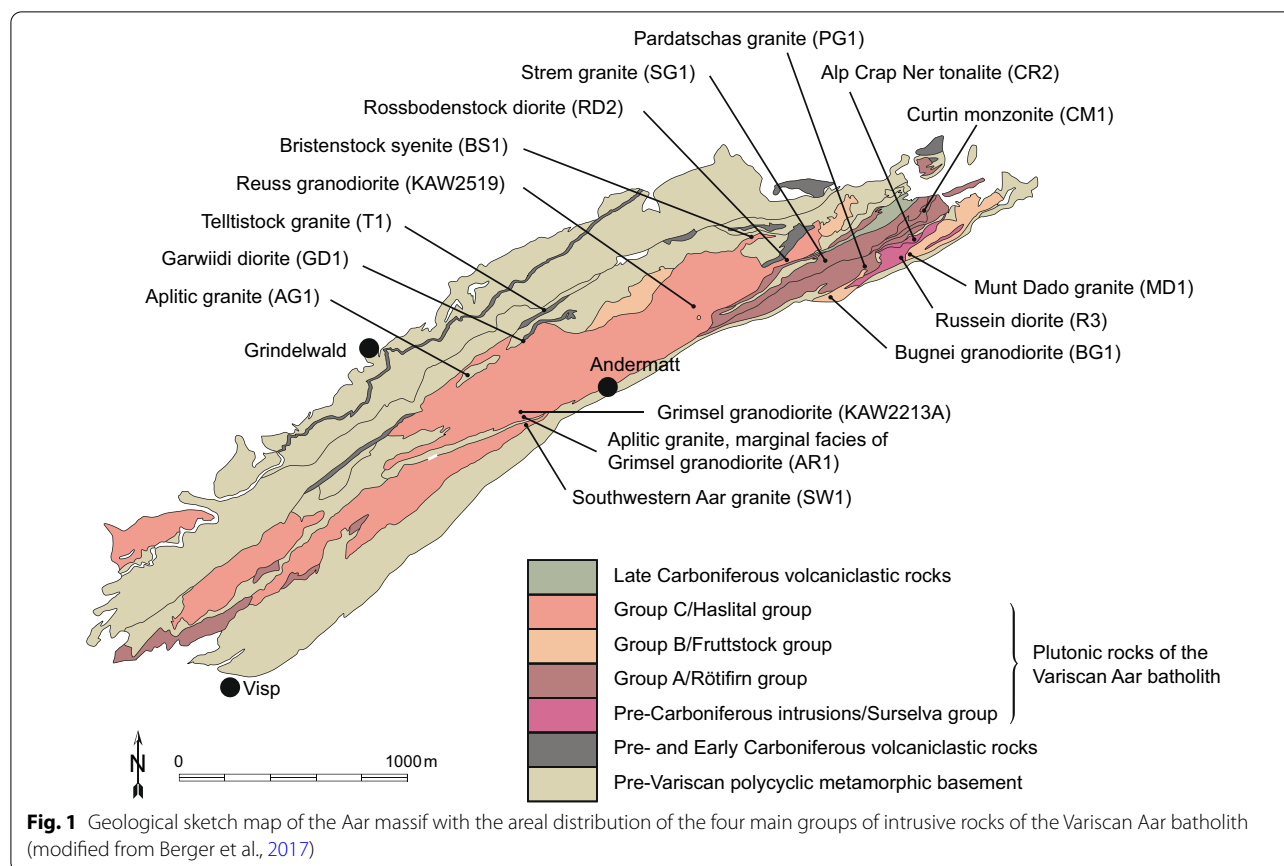
The precise timing of the late Variscan magmatism was a focus of attention in the 1990’s, through a series of U–Pb geochronological studies carried out on the Mont-Blanc, Aiguilles-Rouges and Aar massifs and the Gotthard nappe of the Swiss part of the Helvetic realm (e.g., Bussy et al., 2000; Schaltegger & Corfu, 1992, 1995; Schaltegger & von Quadt, 1990; Sergeev et al., 1995; see also the comprehensive overviews by Schaltegger, 1994, and von Raumer et al., 2013). Unfortunately, there have been no recent geochronological studies, and due to the recent and future geological mapping program to generate the map sheets of the Geological Atlas of Switzerland 1:25,000 (<https://www.swisstopo.admin.ch/en/knowledge-facts/geology/geological-data/geological-maps.html>), it is particularly pertinent to update the geochronology of the Variscan batholith within the Aar massif. Furthermore, many of the igneous lithologies display

sheared and metamorphosed contacts towards surrounding units, which makes it difficult to discern relative age relationships and requires absolute dating. This manuscript reports new U–Pb age determinations on zircon from a series of intrusions, using state-of-the-art laser ablation inductively coupled plasma mass spectrometry (LA-ICPMS) and isotope-dilution thermal ionization mass spectrometry (ID-TIMS) techniques. We also evaluate in this study how chemical abrasion pretreatment of zircon (Mattinson, 2005; Widmann et al., 2019) prior to LA-ICPMS dating affects precision and accuracy of the results. These geochronology data are complemented by zircon trace element concentrations and Hf isotope compositions obtained by LA-ICPMS on the same zircon dated by LA-ICPMS.

These new results allow for (i) comparison of U–Pb dates obtained with different dating techniques over 30 years; (ii) evaluation of analytical strategies of LA-ICPMS and ID-TIMS geochronology of complex magmatic zircon, complicated by Pb-loss and Alpine zircon overprint and growth; (iii) testing the hypothesis of pulsed emplacement of Variscan batholiths (e.g., Schaltegger & Corfu, 1992); and (iv) determination of intrusion ages of previously undated intrusions which lack clear contacts with their wall rock. In addition, the trace element and initial Hf isotope compositions of the zircon analyzed for U–Pb LA-ICPMS enable a new assessment of the geodynamic setting and the potential melt sources of the late Variscan magmatism of the Aar batholith.

2 Geological Setting

The Variscan orogeny is preserved in the Aar massif through medium-to-high grade metamorphism of pre-350 Ma igneous, metamorphic and sedimentary rocks, as well as the Variscan Aar batholith (Fig. 1). Schaltegger et al. (1991), Schaltegger & Corfu (1992) and Schaltegger (1997) distinguished three pulses of magmatism (termed groups A, B, C) through U–Pb geochronology of bulk zircon aliquots. These magmatic pulses were subsequently included in the lithostratigraphic scheme of Berger et al. (2017), and termed the Rötifirn, Fruttstock and Haslital groups, respectively. To be compatible with the Geological Atlas of Switzerland, we introduce these local names alongside a simplified terminology. The first is *Group A/Rötifirn group*, a suite of elongated, lower Carboniferous (ca. 335–330 Ma old) shoshonitic diorites, monzonites, granites and syenites that intruded into deformed



and folded Visean (middle Mississippian) volcano-sedimentary basin sequences at a shallow depth (Cavardiras group of Berger et al., 2016, 2017). Among them are the Curtin monzonite and the Pardatschas granite, however, the most characteristic lithologies of this group are the Giuv syenite and the composite Punteglias intrusion in the south-eastern Aar massif (Schaltegger & Corfu, 1992; Seemann, 1975). The latter was recently re-dated by Gaynor, Ruiz, et al. (2022), who reported a precise weighted mean CA-ID-TIMS U–Pb age of $335.479 \pm 0.041/0.096/0.37$ Ma (X/Y/Z errors after Schoene et al., 2006; Table 2). The second is the *Group B/Fruttsstock group*, which is composed of calc-alkaline diorites, ranging from cumulate-like hornblende gabros to hornblende-diorites and hornblende- or biotite-quartz-monzonite, granodiorites and metaluminous weakly peraluminous I-type granites, which crystallized between 310 and 307 Ma. Intrusions dated in this study are the Düssi diorite east of the Reuss valley, granitic intrusions in the Grueben glacier area in the Grimsel cross section, and the Mont-Dado granite and the Bugnei granodiorite from the eastern Aar massif. The *Group C/Haslital group* comprises the youngest pulse (ca. 304–295 Ma) and is mostly characterized by late-orogenic,

calc-alkaline I-type granites, including the composite Central Aar granite pluton (Grimsel granodiorite with its marginal leucocratic facies, Reuss granodiorite, Southwestern Aar granite), which is the largest exposure of granite in the Aar massif. This pulse of intrusions also includes the Rossboden diorite east of the Reuss valley as well as the small Tellistock granite intrusion in the Trift glacier area. These plutonic rocks partly intrude into Stephanian (uppermost Pennsylvanian/earliest Permian) volcano-sedimentary basins that contain rhyolitic volcanic tuffs, ignimbrites, coarse-grained pyroclastic rocks and volcanic breccias, and fine-grained lahar deposits dated between 303 ± 4 Ma and 299 ± 2 Ma (Berger et al., 2017; Schaltegger & Corfu, 1995). Very likely, the lithologies of the Bristen granite and the Strem granite may be part of this group as well, but unfortunately no significant age determination exists so far.

A new age group of magmatic rocks was identified in the course of this study, comprising two older, pre-Carboniferous intrusions (Russein diorite and Alp Crap Ner tonalite). We introduce here the lithostratigraphic “Surselva group”, which is older than the groups defined by Berger et al., (2016, 2017) and Schaltegger & Corfu (1992).

3 Short description of the sampled lithologies

The following descriptions are taken from Berger et al. (2017), Gisler (2018), Gisler et al. (2020) and Abrecht (2022), as well as from Schaltegger (1990), Schaltegger et al. (1991), Schaltegger & Corfu (1992), Seemann (1975) and from unpublished texts of F. Giovanoli (1:25'000 map sheet Trun, in prep.). The exact location may be found with the help of the Swiss coordinate values in Table 1.

3.1 Pre-Carboniferous intrusions/Surselva group

3.1.1 Russein diorite (R3)

This is an intrusion of a fine-grained, strongly altered and deformed diorite NE of Disentis (Grisons). The Russein diorite forms an elongated, 1.5×13 km-sized intrusive body between the adjacent Munt Dado granite to the south and the pre-Variscan basement (Ausserberg-Avat zone; Berger et al., 2016) as well as Variscan intrusive rocks (Alp Crap Ner tonalite, Pardatschas granite, Bugnei granodiorite) to the north. The magmatic paragenesis has been entirely replaced by Alpine metamorphic mineral assemblage (albite, sericite, Ti and Fe oxides and hydroxides, quartz).

3.1.2 Alp Crap Ner tonalite (CR2)

This tonalite is exposed as a series of elongated lenses (0.9×3 km) of porphyritic tonalite located between the Lumpegna und Punteglias valleys northeast of Disentis (Grisons). They are bordered by pre-Variscan basement gneisses of the Ausserberg-Avat zone (Berger et al., 2016) to the north and Variscan intrusions (mainly the Russein diorite) to the south. The Alpine metamorphic overprint of this unit is characterized by alteration of plagioclase into sericite, and biotite replacement by chlorite.

3.2 Group A/Rötifirn Group

3.2.1 Punteglias granite (KAW676)

The Punteglias granite is a composite intrusion composed of elongated bodies of quartz-monzonite to granite between the Lumpegna and Frisal valleys northeast of Disentis, Grisons, and is exposed over an area of 2.5×15 km. It is bordered by pre-Variscan basement (Ausserberg-Avat zone; Berger et al., 2016) to the south, and the Variscan Curtin monzonite and Strem granite to the north. The sample contains K-feldspar phenocrysts in a dark-colored matrix rich in biotite, amphibole and titanite. The original magmatic fabric

Table 1 Summary of samples localities and LA-ICP-MS ages

Lithology/sample number	Swiss coordinates	Locality	Age
Pre-Carboniferous intrusions/Surselva group			
Russein diorite R3	2711.559/1175.807	Val Russein, Rhine valley	$348.2 \pm 1.2/5.5$ Ma
Alp Crap Ner tonalite CR2	2713.202/1177.546	E of Val Russein	$339.8 \pm 2.1/8.6$ Ma
Group A/Rötifirn group			
Curtin monzonite CM1	2714.046/1180.850	Disentis	$327.6 \pm 1.6/3.8$ Ma
Pardatschas granite PG1	2707.143/1174.703	Truaisch above Disentis	$329.9 \pm 1.9/5.2$ Ma
Group B/Fruttsstock group			
Düssi diorite KAW3210		Bottom of Brunni valley, upper Maderaner valley	$307.1 \pm 1.6/5.3$ Ma
Aplitic granite AG1	2662.200/1162.210	Grueben glacier, Hasli valley	$307.4 \pm 2.0/4.4$ Ma
Munt Dado granite MD1	2712.247/1176.083	Val Russein	~ 308.8 Ma
Bugnei granodiorite BG1	2703.345/1171.362	Above Bugnei, Sedrun	~ 311 Ma
Group C/Haslital group			
Grimsel granodiorite KAW2213A	2669.000/1157.500	Above Grimsel lake	$297.2 \pm 1.0/4.3$ Ma
Reuss granodiorite KAW2519	2687.660/1167.830	Schöllenen gorge, Reuss valley	$298.1 \pm 1.1/4.8$ Ma
Southwestern Aar granite SW1	2669.609/1156.976	South of Grimsel pass	~ 296 Ma
Garwiidi diorite GD1	2668.366/1166.355	Ofenhorn, Hasli valley	$295.6 \pm 2.0/7.9$ Ma
Aplitic granite (marginal facies of Grimsel granodiorite) AR1	2668.949/1157.361	North of Grimsel pass	$299.2 \pm 1.4/6.8$ Ma
Rossbodenstock diorite RD2	2698.070/1175.383	Etzli valley, Rossbodenstock	$298.6 \pm 1.0/3.6$ Ma
Telltistock granite T1	2671.835/1170.486	Trift glacier	$301.2 \pm 1.5/5.0$ Ma
Samples not assigned to one of the above groups			
Bristenstock syenite BS1	2694.385/1178.280	Bristenstock	~ 304 Ma (?)
Strem granite SG1	2702.959/1175.236	Piz Gendusas, Val Segnas	no age

has been overprinted by moderate alpine deformation, during which Alpine biotite, albite, epidote and sericite crystallized.

3.2.2 Curtin monzonite (CM1)

The Curtin monzonite is a 1×9 km-sized band of syenite to quartz-monzonite, which has a contact with the Punteglias granite intrusion along its northern border and is located between Lumpegna and Punteglias valleys north-east of Disentis (Grisons). It shows a transitional mixing zone with the northern adjacent Strem granite. The intrusion has retained magmatic fabrics within its contact regions, which suggests that it was emplaced after the intrusion of the Strem granite.

3.2.3 Pardatschas granite (PG1)

This is a 2×27 km large, elongated body of strongly deformed leucocratic granite located between the Strem granite and the pre-Variscan basement gneisses of the Aussberg-Avat zone (Berger et al., 2016). It extends from the area west of Oberalp pass to northeast of Disentis (Grisons) at the southern margin of the Aar massif. Preserved crosscutting relationships indicate that it is younger than the Punteglias granite. While current exposures suggest that the unit originally had a porphyritic texture, the magmatic minerals have been largely replaced by an Alpine mineral assemblage. In the center of the intrusion the magmatic textures are well-preserved and the granite contains swarms of magmatic enclaves of gabbroic, dioritic to syenitic composition.

3.3 Group B/Fruttsstock Group

3.3.1 Düssi diorite (KAW3120)

This is a compositionally heterogeneous elongated intrusion (1×5 km) exposed in the Brunni valley (upper Madraner valley, Uri), composed of dark amphibole gabbro to diorite, as well as monzodiorites. The intrusive body is part of a larger intrusive complex with the Brunni granite and is strongly interfingered with the surrounding pre-Variscan basement of the Sustenhorn zone (Berger et al., 2016) on both its southwestern and northeastern margins. The analyzed sample is a biotite-bearing monzodiorite with interstitial K-feldspar, which was previously studied by Schaltegger et al. (1991) and Schaltegger & Corfu (1992).

3.3.2 Leucocratic aplitic granite (AG1)

Members of this granite unit form a series of several small intrusions (up to 2500m^2) and dykes of fine-grained and undeformed grey aplitic granites. These intrusions crosscut the pre-Variscan gneisses of the Sustenhorn zone north of the Central Aar granite (Berger et al., 2016) in the region west of the Grueben glacier (Grimsel cross

section, Bern). Dark patches are interpreted as relics of entirely altered cordierite and point to an anatectic formation of these melts from the metasedimentary basement rocks.

3.3.3 Munt Dado granite (MD1)

This is an elongate amphibole and biotite-bearing granite intrusion, exposed over approximately 16 km between Disentis and Brigels (Grisons) bordering the Russein diorite in the north. The intrusion does not indicate clear relative age relationships towards other members of the Aar batholith. To the south, the Munt Dado granite is bounded by the shear-zones that mark the southern border of the Aar massif. The Alpine deformation of this unit is highlighted by the presence of abundant secondary chlorite and altered feldspar.

3.3.4 Bugnei granodiorite (BG1)

This granodiorite is a lens-shaped and strongly sheared intrusion, exposed over approximately 8 km occurring in the Rhine valley between Sedrun and north of Disentis (Grisons) at the southern edge of the Aar massif. It is isolated from the surrounding Pardatschas granite and Russein diorite by Alpine shear-zones. The central part has preserved magmatic textures and partly the magmatic mineral assemblage.

3.4 Group C/Haslital Group

3.4.1 Grimsel granodiorite (KAW2213A)

The Grimsel granodiorite is a 3–4 km long, lens-shaped body of dark, mostly strongly foliated, coarse-grained granodiorite. It is a phase of the broader Central Aar granite intrusion north of the Grimsel pass (Bern). It contains abundant quartz-dioritic enclaves and is crosscut by numerous aplite dykes. It was described and studied by Schaltegger (1990), and U–Pb ages have previously been published by Schaltegger & von Quadt (1990) and Schaltegger & Corfu (1992).

3.4.2 Reuss granodiorite (KAW2519)

This coarse-grained granodiorite intrusion with moderate Alpine foliation is a part of the Central Aar granite intrusion and occurs in the Schöllenen gorge (Uri). Detailed description of this unit can be found in Schaltegger (1990), and U–Pb ages in Schaltegger & von Quadt (1990), and Schaltegger & Corfu (1992).

3.4.3 Southwestern Aar granite (SW1)

This leucocratic and coarse-grained to porphyritic granite was formerly called “Southern Aar granite” and forms a 28 km long intrusion between the Rhone and the Aletsch glaciers (Valais). It is separated from the Grimsel granodiorite south of the Grimsel pass by a thin layer

of pre-Variscan gneisses and borders similar basement rocks to the south. Structurally and compositionally it is identical to the Central Aar granite s. str., north to the Grimsel granodiorite in the Grimsel pass traverse.

3.4.4 Garwiidi diorite (GD1)

The Garwiidi diorite forms a series of three small-sized (only a few 100m²) dioritic intrusions of texturally undeformed, biotite-bearing amphibole quartz diorites with An-rich plagioclase and traces of K-feldspar. They are located east of the Grimsel pass road (Bern) in the area of the Ofenhoren. The primary mineralogy was strongly altered by Alpine fluid percolation. The diorites cross-cut pre-Variscan migmatites of the Sustenhorn zone (Berger et al., 2016) and contain xenolith enclaves of these migmatites. These intrusions share a contact with the late-Variscan volcano-sedimentary basin sequences (Diechtermgletscher formation).

3.4.5 Aplitic granite (marginal facies of the Grimsel granodiorite; AR1)

Along the Grimsel pass road (Bern), a 100 to 200 m thick band of a leucocratic biotite-granite can be observed along the southern border of the Grimsel granodiorite. It shows strong and pervasive cataclastic deformation, hosts abundant mafic dykes and enclaves. Exposure of this phase is only present a few km along the western and the eastern portions of the Grimsel profile.

3.4.6 Rossbodenstock diorite (RD2)

This is an elongated intrusive body (0.2 × 2.5 km) composed of massive, coarse-grained biotite-amphibole diorite to quartz diorite in the Etzli valley east of the Reuss valley (Uri). During the Alpine metamorphic cycle, magmatic fabrics and minerals are increasingly overprinted towards the margins of the intrusion. In particular, this affected both the contacts towards the late Variscan volcano-sedimentary sequence (Tscharren formation), as well as the contacts with the central Aar granite.

3.4.7 Telltistock granite (T1)

The Telltistock granite forms an elongated 0.3 × 4 km intrusion of leucocratic granite in the region of the Trift glacier east of the Grimsel pass cross section (Bern). It shows a characteristic, pervasive cataclastic deformation together with intense alteration of the primary mineralogy and the formation of Fe-oxides and hydroxides, clays, epidote, chlorite and calcite. It is in contact with the late-Variscan volcano-sedimentary sequences along its southern border, and with the pre-Variscan gneisses of the Ferden-Guttannen zone in the north (Berger et al., 2016).

3.5 Lithologies for which no age was obtained

3.5.1 Bristenstock syenite (BS1)

This is a 170 × 800 m lens of quartz-bearing amphibole syenite exposed within the pre-Variscan gneisses of the Sustenhorn zone (Berger et al., 2016) north of the Central Aar granite (Bristenstock, Reuss valley, Uri). The magmatic fabric is strongly deformed within the outer regions of the intrusion, and primary igneous mineralogy was significantly altered to a metamorphic assemblage presumably during the Alpine orogeny.

3.5.2 Strem granite (SG1)

The Strem granite is an elongated body of a grey, porphyritic granite with well-defined foliation in contact with the Central Aar granite. It extends from the Oberalp pass to the region northeast of Disentis (Grisons) over approximately 30 km, without any exposures of cross cutting relationships that could define its relative age within the broader assembly of the Aar Massif batholith. Unfortunately, the Strem granite as well as the Southwestern Aar granite (see above) were previously called “Southern Aar granite”, leading to some confusion. U–Pb zircon analyses of Schaltegger & Corfu (1992) revealed the existence of abundant inheritance in its zircon, which was interpreted to reflect a crustal source for magma genesis.

4 Methods

4.1 Sample separation

The sample localities of the fifteen studied intrusions are indicated in Fig. 1 and Table 1. Samples were crushed and milled to a grain size < 300 µm in a tungsten-carbide mill. Heavy minerals were separated using a Holman-Wilfley shaking table, the non-magnetic portion was then separated using a Frantz magnetic separator, and finally concentrated into a high-density fraction using methylene iodide ($D = 3.3 \text{ g/cm}^3$). In addition to these samples, four samples previously dated in Schaltegger & von Quadt (1990) and Schaltegger & Corfu (1992) were also reanalyzed (KAW676, KAW3120, KAW2213A and KAW2519), using the zircon separates previously prepared for those studies. These were large, 35 kg-sized samples, which yielded milligram amounts of non-magnetic zircon. A representative number of high-quality grains (30–50 per sample) were selected under a binocular from the heavy mineral fractions, preferring transparent grains without milky or turbid zones, and avoiding grains with cracks and/or inclusions. The zircon grains were mounted in an epoxy resin, polished to approximately equatorial sections using SiC paper and diamond paste, and carbon coated for cathodo-luminescence imaging.

4.2 Cathodo-luminescence (CL) imaging

Panchromatic CL images were taken of each selected zircon using the secondary electron microscope (SEM) at the University of Geneva to study the internal structures of zircons to distinguish pristine magmatic domains with oscillating zoning from zones with secondary alteration features. The high-resolution images subsequently served as a base for placing the laser spot for trace element analyses, and U–Pb and Hf isotope analyses, as well as a help with the interpretation of the obtained U–Pb ages. The carbon coating was removed prior to LA-ICP-MS U–Pb dating. CL images of all dated grains are stored on the Yareta FAIR server of University of Geneva at doi:10.26037/yareta.

4.3 Chemical abrasion (CA)

Zircon aliquots from samples that yielded a sufficiently high number of optically clear and inclusion-free crystals were pre-treated by chemical abrasion before analysis by LA-ICPMS or ID-TIMS dating techniques. This pre-treatment removes radiation-damaged domains within the zircon prior to analysis, as these domains are susceptible to open system behavior and as a result may have suffered from loss of radiogenic Pb, as well as mineral inclusions. Individual zircon crystals were annealed in a muffle furnace at 900 °C for 48 h (Mundil et al., 2004). The annealed zircon grains then underwent step-wise chemical abrasion at 210 °C for 4–12 h in concentrated HF in 3 ml Savillex beakers within a Parr digestion vessel (Mattinson, 2005; Widmann et al., 2019). This procedure was stopped before complete dissolution was achieved, and sufficient zircon material was left for analysis. The duration of the partial dissolution step is therefore depending on the radiation dose of the respective zircon population. Zircon that underwent this pre-treatment were washed 4 times in ultrapure H₂O prior to mounting in epoxy resin for LA-ICPMS dating.

4.4 LA-ICPMS U–Pb dating

The U–Pb analyses were carried out using a sector-field, single-collector Element XR ICP-MS interfaced to a RESolution SE 193-nm excimer ablation system (University of Lausanne). A laser spot diameter was set at 20 µm. A low energy density of 2.5 J/cm² and a repetition rate of 5 Hz were used to minimize isotopic fractionation (Ulianov et al., 2012). The relative sensitivity factors were calibrated through repeated measurements of the untreated GJ-1 reference zircon (applying the CA-ID-TIMS ²⁰⁶Pb/²³⁸U age of 600.34 Ma from Boekhout et al., 2012; Ulianov et al., 2012). During calibration, this age was reproduced with an uncertainty of 0.18 Ma (2σ, n=263, MSWD=0.93; Additional file 2: Fig S1a), while a smaller suite of analyses of chemically abraded GJ-1

showed slightly more scatter and yielded a ²⁰⁶Pb/²³⁸U age of 600.27 ± 0.67 Ma (95% c.l., n=96, MSWD=1.5; Additional file 2: Fig. S1b). The accuracy of the analytical setup was tested by repeated analysis of reference material Plešovice as a secondary standard (ID-TIMS ²⁰⁶Pb/²³⁸U ages are 337.13 ± 0.37 Ma, Sláma et al., 2008, and 336.96 ± 0.25 Ma, Widmann et al., 2019), which yielded a ²⁰⁶Pb/²³⁸U age of 337.03 ± 0.27 Ma for untreated grains (2σ, N=64, MSWD=1.19; Additional file 2: Fig. S1c) and a ²⁰⁶Pb/²³⁸U age of 337.74 ± 0.31 Ma for chemically abraded grains (2σ, N=27, MSWD=1; Additional file 2: Fig. S1d). Typically, a block of 20 analyses included 8 primary standard (GJ-1) measurements (positions 1–4 at the beginning and 17–20 at the end of the block, respectively, indicated in Additional file 3: Table S1c, second row), two analyses of the secondary standard Plešovice (positions 15, 16; Additional file 3: Table S1c), and analysis of 10 unknowns. In case of LA-ICPMS analysis of chemically abraded zircon, both reference zircon standards and unknowns underwent the same pre-treatment to avoid matrix effects from differential ablation rates between untreated and chemically abraded aliquots (Crowley et al., 2014). No common lead corrections were applied to results due to the presence of ²⁰⁴Hg in the system. All reported LA-ICPMS ages in figures, tables and text are ²⁰⁶Pb/²³⁸U ages, and these data were plotted using IsoplotR (Vermeesch, 2018). All U–Pb isotope diagrams are found in the supplementary materials, as (i) ²⁰⁶Pb/²³⁸U age scatter plots, and (ii) Wetherill Concordia diagrams (Additional file 2: Figs. S2 to S19). Uncertainties of weighted ²⁰⁶Pb/²³⁸U mean ages were multiplied by √MSWD and are reported at 95% c.l. limits, when the MSWD was outside the acceptable limits for a given number of analyses (Wendt & Carl, 1991).

Given the excess scatter in all dated rocks, even after removal of anomalously old or young analyses, the reported weighted mean ages of the selected population of analyses may not be accurate within uncertainty determined purely from data scatter, even for uncertainties expanded by √MSWD at 95% c.l. While this method is commonly adopted to calculate the uncertainty for the measurement of unknowns, it does not incorporate all sources of potential error in LA-ICPMS data reduction. During the analysis sessions, the primary standard GJ-1 was measured very reproducibly (Additional file 2: Fig. S1a), adding a minimal uncertainty to the relative sensitivity factors further applied to the samples to quantify their age. However, the variation of the relative sensitivity factor between the different zircons may be a significant additional source of uncertainty. This latter uncertainty component has been shown to be ±1–3% of an individual age based on round-robin experiments of untreated reference zircon materials (e.g., Allen & Campbell, 2012;

Horstwood et al., 2016; Klötzli et al., 2009). However, this error cannot be reliably quantified nor propagated into our uncertainty. This leads to overly precise data that may potentially be inaccurate within their uncertainty limits. For this study, we made a conservative estimate of uncertainty by using half of the difference between the oldest and youngest grains in the selected population of dates ($\Delta t/2$ of the selected dates), as recently applied to scattering CA-ID-TIMS and LA-ICPMS datasets (e.g., Gaynor, Ruiz, et al., 2022; Gaynor, Svensen, et al., 2022; Rosera et al., 2021). We report this as “extended error” in the format $[X] (95\% \text{ c.l.}) / [Y] (\text{extended error})$ in Figs. 3 and 8, in Additional file 2: Figs. S3 to S18, as well as in Additional file 3: Table S1. This enhanced error, even though probably overestimated, allows for a more accurate age interpretation from scattering U–Pb dates, which is more important than apparent precision.

4.5 CA-ID-TIMS U–Pb dating

Zircon fragments remaining after chemical abrasion were leached on a hotplate at 80 °C in 6 N HCl for at least 12 h, followed by further cleaning through four rounds of 7 N HNO₃ in combination with ultrasonication. Individual cleaned zircon crystals or sub-grain fragments were then loaded into individual 200 µl Savillex microcapsules, spiked with the EARTHTIME ²⁰²Pb–²⁰⁵Pb–²³³U–²³⁵U tracer solution (calibration version 3; Condon et al., 2015; McLean et al., 2015) and dissolved with approximately 70 µl HF and trace HNO₃ in a Parr digestion vessel at 210 °C for 48 h. Following dissolution, samples were dried down and converted to a chloride by placing them back in the oven overnight in 6 N HCl. The samples were then dried down again and re-dissolved in 3 N HCl and purified to U and Pb through anion exchange column chromatography using H₂O and HCl. Once purified, the U and Pb fractions were combined in cleaned 7 ml Savillex beakers and dried down with trace H₃PO₄.

Uranium and lead isotope analyses were done on an IsotopX Phoenix TIMS at the University of Geneva. Chemically purified U–Pb aliquots were loaded onto outgassed zone-refined Re ribbon filaments with a Sigel emitter for analysis. Lead measurements were made in dynamic mode using a Daly photomultiplier, while uranium was measured as an oxide in static mode using Faraday cups coupled to 10¹² Ω resistors. The ¹⁸O/¹⁶O oxygen isotope ratio in uranium oxide was determined to be 0.00205 based on replicate measurements of the U500 standard. For samples spiked with the EARTHTIME ²⁰²Pb–²⁰⁵Pb–²³³U–²³⁵U tracer solution, mass fractionation of Pb was corrected using a ²⁰²Pb/²⁰⁵Pb ratio of 0.99923913 ± 0.00026555 (1σ) (Condon et al., 2015). For all analyses, U mass fractionation was corrected using a ²³⁸U/²³⁵U ratio of 0.995062 ± 0.000108 (2σ) and

a ²³⁸U/²³⁵U ratio of 137.818 ± 0.045 (2σ) (Condon et al., 2015; Hiess et al., 2012). All common Pb was considered to be laboratory blank for zircon and was corrected using the isotopic composition of the Pb blank at the University of Geneva (Schaltegger et al., 2021). All data were processed with the Tripoli and Redux U–Pb software packages (Bowring et al., 2011; McLean et al., 2011). All zircon ages were corrected for initial ²³⁰Th disequilibrium by assuming a U/Th ratio of the magma of 3.5. Data are reported in Additional file 4: Table S2.

During the period of this project, synthetic ET100 solutions were run to control the accuracy of the data and yielded a mean ²⁰⁶Pb/²³⁸U age of 100.1664 ± 0.0057 Ma (MSWD = 2.8; n = 17), which agrees with the proposed value of 100.173 ± 0.003 Ma (MSWD = 2.6; n = 67) in Schaltegger et al. (2021).

4.6 LA-ICPMS trace element analysis

The same Element XR single-collector (LA-SF-ICPMS) and RESOLUTION SE 193-nm excimer ablation system as used for the U–Pb dating at the University of Lausanne analysed trace elements in zircon (Sr, Y, Nb, Ba, La, Ce, Pr, Nd, Sm, Eu, Gd, Tb, Dy, Ho, Er, Tm, Yb, Lu, Hf, Ta, Th, U) during a separate analytical session, with a spot diameter of 50 µm, sometimes reduced to 24 µm in small zircon grains. A SRM 612 glass was used for standardization using the same spot size as for unknowns. The ²⁹Si intensity was taken as an internal standard to correct for differences of ablation yield between zircon and SRM612 glass. Element concentrations were based on the stoichiometric ²⁹Si concentration of 33 wt.% in zircon. All data are reported in Additional file 5: Table S3. Uncertainties were estimated on the basis of the repeatability of 16 analyses of the GJ-1 reference zircon and are reported as 1 sigma standard deviation in Additional file 6: Table S4.

4.7 Initial Hf isotope analysis by LA-ICP-MS

In-situ Hf isotope measurements were carried out on a Thermo Neptune Plus multi-collector-ICP-MS coupled to a NWR 193 HE laser ablation system at the University of Geneva. Ablation was performed at a fluence of ~5 J/cm², a repetition rate of 5 Hz and a spot size of 40 µm. Helium was used as a carrier gas for the ablated particles and mixed with a small amount of N₂ before entering the Ar-plasma torch to increase sensitivity. Measurements were performed at low mass resolution over 120 cycles of 1 s for standards and between 30 and 120 cycles for samples (depending on the thickness of the zircon analyzed). At the beginning and at the end of the session, and every ~20 sample measurements, Mud Tank (¹⁷⁶Hf/¹⁷⁷Hf = 0.282507; Woodhead & Hergt, 2005), Plešovice (¹⁷⁶Hf/¹⁷⁷Hf = 0.282482; Slama et al., 2008), GJ-1 (¹⁷⁶Hf/¹⁷⁷Hf = 0.282000; Morel et al., 2008),

and synthetic MUN ($^{176}\text{Hf}/^{177}\text{Hf}=0.282135$; Fisher et al., 2014) zircon standards were measured in order to evaluate the offset of the measured values to reference values. Blanks were also acquired (120 cycles) at the same intervals as the zircon standard measurements, but without ablation.

Data were reduced off-line using an excel spreadsheet and consisted of blank subtractions, removing the isobaric interference of ^{176}Lu and ^{176}Yb on mass 176 (e.g., Fisher et al. 2014) and correcting the resulting $^{176}\text{Hf}/^{177}\text{Hf}$ ratio for mass bias using an exponential law (Albarède et al., 2004). The βHf and βYb mass bias coefficients were calculated from the measured $^{179}\text{Hf}/^{177}\text{Hf}$ and $^{173}\text{Yb}/^{171}\text{Yb}$ with the reference values of Patchett & Tatsumoto (1980) ($^{179}\text{Hf}/^{177}\text{Hf}=0.7325$) and Thirlwall & Anczkiewicz (2004) ($^{173}\text{Yb}/^{171}\text{Yb}=1.1234$). Isobaric interferences of ^{176}Yb and ^{176}Lu with ^{176}Hf were corrected using $^{176}\text{Yb}/^{173}\text{Yb}=0.786954$ and $^{176}\text{Lu}/^{175}\text{Lu}=0.02645$ respectively (Thirlwall & Anczkiewicz, 2004). Time resolved $^{176}\text{Hf}/^{177}\text{Hf}$ plots were used to detect any heterogeneities like inclusions or different domains (e.g., inherited cores) with different $^{176}\text{Hf}/^{177}\text{Hf}$ ratios. Only non-perturbed spectra were retained. Initial $^{176}\text{Hf}/^{177}\text{Hf}$ ratios and initial ϵHf were calculated using the $^{206}\text{Pb}/^{238}\text{U}$ date of the respective crystal, the CHUR parameters of Bouvier et al. (2008) ($^{176}\text{Hf}/^{177}\text{Hf}=0.282785$ and $^{176}\text{Lu}/^{177}\text{Hf}=0.0336$) and $\lambda^{176}\text{Lu}=1.87 \times 10^{-11} \text{ a}^{-1}$ (Söderlund et al., 2004).

The reproducibility of the measured standards (2SD), including the offsets with respect to their nominal values, reported above during the analytical session was <1.5 epsilon units (<1 epsilon unit excluding offset). This reproducibility was propagated into the uncertainties of unknowns, such that the uncertainty of analysis of unknown zircons included internal uncertainty during the run, standard reproducibility, and standard offset from nominal values. All values are reported in Additional file 7: Table S5.

5 Results

5.1 Optical characteristics and internal growth textures from CL imaging

Most of the Variscan intrusions in the Aar massif contain variable proportions of porous, turbid white to milky white-opaque zircon with high U concentrations (Grünenfelder, 1963; Schaltegger & von Quadt, 1990). This proportion of milky zircon is highest in the highly evolved, very SiO_2 -rich parts of the Central Aar Granite along the northern border (Schaltegger & von Quadt, 1990). The growth history of magmatic zircon can be qualitatively assessed through CL imaging. CL images of all zircon crystals analyzed within this study can be accessed on the Yareta FAIR server of University of Geneva, at doi:10.26037/yareta. A short description of

the main features observed in CL imagery may be found in the Additional file 1. Typical zircon textures from both untreated and chemically abraded zircon grains are compiled in the CL images shown in Fig. 2.

The selected grain of sample KAW676 shows typical combination of sector and oscillatory zoning, common for intermediate to mafic rocks and for most of the analyzed zircon (see the grains of BG1, CM1 for other examples; see Gaynor, Ruiz, et al., 2022 for further CL imagery of sample KAW676). The margins may show some signs of alteration and the low-CL core may possibly contain a xenocrystic component or inclusion of a different mineral phase. The acicular zircon from KAW2213A is dominated by oscillatory zoning, indicating different magmatic growth pulses. The selected KAW2519 grain is a good example for secondary replacement of primary, oscillatory zoned growth zones by secondary zones with non-planar textures. Such replacement can also be observed along the margins of the diorite grain from KAW3120, while its interior part shows simple planar zoning. The grain from AR1 shows a low-CL core that is epitactically overgrown by a quasi-homogeneous

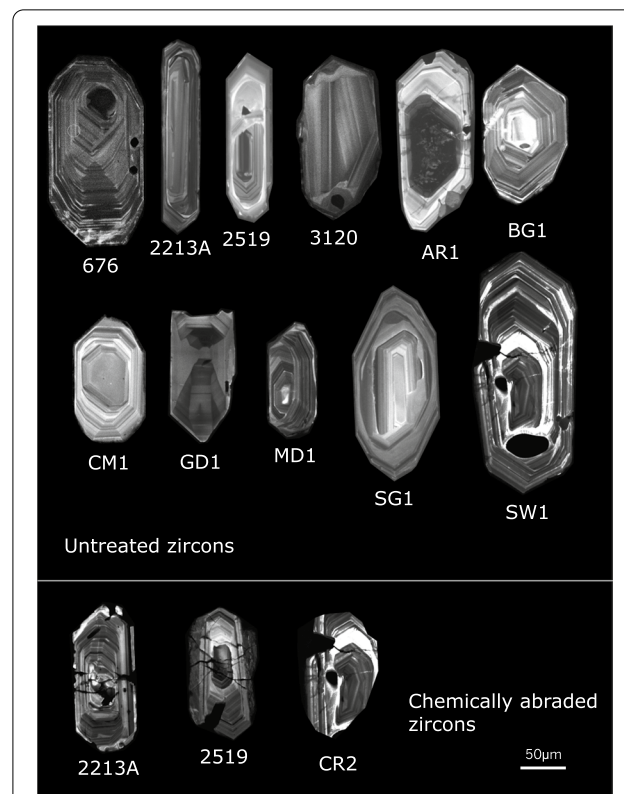


Fig. 2 Representative CL images from some of the dated lithologies. Upper panel, untreated grains; lower panel, chemically abraded grains. Full set of CL images of all analyzed zircon grains may be accessed at doi:10.26037/yareta

high-CL zone and a further oscillatory zone; the core cannot necessarily be considered as xenocrystic, but instead may represent different growth episodes at different magma composition. The same may possibly apply for the grain of BG1, however, it seems that the core texture may be truncated and therefore may be older. The apparent core of CM1 is interpreted as an effect of non-equatorial cutting of the grain, exactly parallel to a {100} or {010} face. The zircon of GD1 shows a CL texture typical of diorites, dominated by sector zoning. The grain of MD1 was selected because it shows a clear distinction between two growth episodes with different textural characteristics. Since the younger domain to the right of the grain is oscillatory zoned, we interpret both as magmatic growth zones. Another example is grain SG1, where a presumably xenocrystic core is truncated by subsequent younger growth zones. A xenocrystic origin of the core is suspected as well for the grain from SW1. In summary, the selected CL images represent the big variety of internal growth textures, xenocrystic central domains of the grains, major volumes of magmatically grown zircon zones, in addition to secondary overprinting of (late-) magmatic or post-magmatic zircon growth or alteration. From this finding alone, we would expect that U–Pb system of these zircon grains is complex. CL imaging of chemically abraded grains in the lower panel of Fig. 2 demonstrates the effects of chemical abrasion on grains of samples KAW2213A, 2519 and CR2, removing distinct zones within the zircon rather than dissolving rims preferentially.

5.2 LA-ICPMS U–Pb geochronology

The results of LA-ICPMS dating are listed in Additional file 4: Table S2, in Additional file 2: Figures S3 to S19, and are summarized as $^{206}\text{Pb}/^{238}\text{U}$ date ranked plots in Fig. 3. Each individual analytical spot from Additional file 3: Table S1 is labeled on the respective CL images stored at doi:10.26037/yareta. All results are given with two uncertainties, at the 95% c.l. (enhanced by $\sqrt{\text{MSWD}}$) with an extended error ($\Delta t/2$ for the selected plateau). The results are presented below in the order of four identified magmatic pulses:

Pre-Carboniferous intrusions/Surselva group: we introduce this new magmatic pulse within the Aar massif, which is older than the groups defined by Berger et al., (2016, 2017).

5.2.1 Russein diorite (sample R3)

From a total of 24 analyses, a subset of 19 (15 untreated, 3 CA for 8 h) was used to calculate a mean $^{206}\text{Pb}/^{238}\text{U}$ age of $348.2 \pm 1.2/5.5$ Ma (MSWD = 1.4; Fig. 3A). One older outlier and five outlying younger dates were excluded before the calculation of the mean age.

5.2.2 Alp Crap Ner tonalite (sample CR2)

A total of 26 analyses were obtained, 16 from untreated zircon grains, 10 from 8 h chemically abraded grains. The two subsets of data are not significantly different and both show excess scatter (339.8 ± 2.9 Ma, MSWD = 3.5 for untreated, 339.7 ± 3.5 Ma, MSWD = 2.6 for CA grains). Four analyses (2 untreated, 2 CA) were significant outliers to these populations, and were not considered for calculation of a mean age. These two overlapping populations yielded a weighted mean $^{206}\text{Pb}/^{238}\text{U}$ age of $339.8 \pm 2.1/8.6$ Ma (MSWD = 3.1; Fig. 3A), which we take as the best estimate for the zircon crystallization of this sample.

5.3 Group A/Rötifirn group

5.3.1 Curtin monzonite (sample CM1)

A weighted mean $^{206}\text{Pb}/^{238}\text{U}$ age of $327.6 \pm 1.6/3.8$ Ma (95% c.l., MSWD = 2.3) was calculated from 12 analyses of untreated zircon. Five analyses were rejected because they were anomalously young and old, as well as normally and inversely discordant (Fig. 3B).

5.3.2 Pardatschas granite (sample PG1)

A weighted mean $^{206}\text{Pb}/^{238}\text{U}$ age of $329.9 \pm 1.9/5.2$ Ma (95% c.l., MSWD = 3.0) was calculated from 10 analyses of untreated zircon (Fig. 3B), while 7 other analyses range down to 260 Ma and were excluded from this calculation.

5.4 Group B/Fruttstock group

5.4.1 Düssi diorite (sample KAW3120)

A mean $^{206}\text{Pb}/^{238}\text{U}$ age of $307.1 \pm 1.6/5.3$ Ma (95% c.l., MSWD = 3.3) was calculated from 17 concordant analyses from untreated zircon (Fig. 3C).

5.4.2 Leucocratic aplitic granite, Grueben glacier (sample AG1)

This lithology contained small zircon crystals that were at maximum 50 μm long, and data from these grains yielded a weighted mean $^{206}\text{Pb}/^{238}\text{U}$ age of $307.4 \pm 2.0/4.4$ Ma (95% c.l., MSWD = 4.2), calculated from 11 analyses with a significant amount of scatter (Fig. 3C). One analysis (Fe16b08) off a xenocrystic core had a $^{206}\text{Pb}/^{238}\text{U}$ age of 484 Ma.

5.4.3 Munt Dado granite (sample MD1)

A significant number of transparent and inclusion-free zircon crystals could be separated from this sample, allowing for analysis of both untreated (18 grains) and chemically abraded (16 grains) zircon aliquots (Fig. 3C). Both data sets show large excess scatter, their respective mean $^{206}\text{Pb}/^{238}\text{U}$ ages are 308.3 ± 1.8 Ma (MSWD = 6.2) for untreated and 309.4 ± 2.3 Ma (MSWD = 7.9) for 8 h chemically abraded zircon. Any outlier rejection would

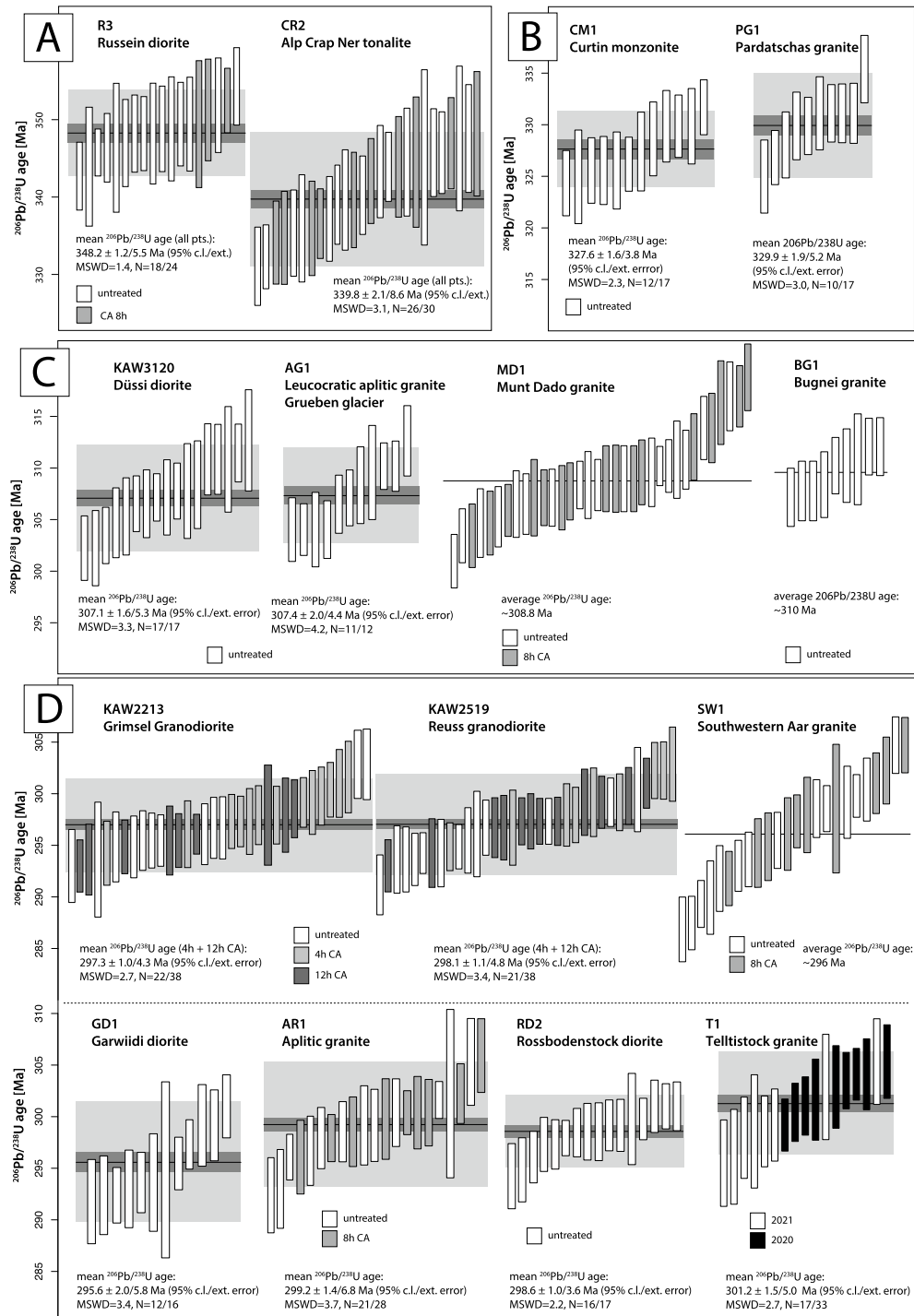


Fig. 3 Age-ranked order plots of LA-ICP-MS dates: **A** Pre-Carboniferous intrusions/Surselva group; **B** Samples of Group A/Rötifirn group; **C** Samples of Group B/Fruttlstock group; **D** Samples of Group C/Haslital group

be subjective and not statistically sound, therefore we prefer to propose an indicative average $^{206}\text{Pb}/^{238}\text{U}$ age value of 308.8 Ma for this sample. The CL image in Fig. 2 may indicate the presence of two distinct growth episodes, which, however, could not be resolved from the scattering data nor from their chemical composition.

5.4.4 Bugnei granodiorite (sample BG1)

The 18 grains analyzed yielded dates that scatter between 227 and 459 Ma with minimal overlap, which does not allow calculation of an age. Eleven concordant analyses indicate an approximate age of 311 Ma (Fig. 3C).

5.5 Group C/Haslital group

5.5.1 Grimsel granodiorite (sample KAW2213A)

Analyses of untreated zircon (16 analyses), of 4 h chemically abraded zircon (12 analyses) and of 12 h chemically abraded zircon (10 analyses) were carried out. Their rank order plot in Fig. 3D shows no systematic distribution of U–Pb dates between these three data sets (Fig. 3D). The three $^{206}\text{Pb}/^{238}\text{U}$ ages of these separate aliquots are 296.3 ± 1.8 Ma (MSWD = 3.5; N = 12, after removal of four outliers with much too old/young date) for untreated zircon, 298.2 ± 1.2 Ma (MSWD = 2.0; N = 13) for zircon which had been pretreated using 4 h of chemical abrasion, and 295.9 ± 1.0 Ma (MSWD = 1.6; N = 9) for zircon which had undergone 12 h of chemical abrasion. There is significantly more scatter in the ages of the untreated sample compared to the zircon which had undergone chemical abrasion, best highlighted by their respective MSWD values. This indicates that the chemical abrasion pretreatment allowed for more reproducible measurements for this sample. We interpret a weighted mean $^{206}\text{Pb}/^{238}\text{U}$ age of $297.3 \pm 1.0/4.3$ Ma (95% c.l., MSWD = 2.7; N = 22) calculated from the analyses of 4 h and 12 h chemically abraded zircon as the crystallization age of zircon in this sample (Fig. 3D).

5.5.2 Reuss granodiorite (sample KAW2519)

A total of 38 spot analyses has been carried out from 17 untreated grains, 9 grains which had been chemically abraded for four hours, and 12 grains that had undergone twelve hours of chemical abrasion. After removal of four anomalously old or young analyses, the remaining 13 analyses of untreated zircon yield a weighted mean $^{206}\text{Pb}/^{238}\text{U}$ age of 295.2 ± 1.3 Ma (MSWD = 2.4), while the aliquots which underwent 4 h and 12 h of chemical abrasion yield dates of 298.8 ± 2.2 Ma (MSWD = 4.1) and 297.6 ± 1.4 Ma (MSWD = 2.8), respectively. There is no systematic age difference between untreated and chemically abraded zircon aliquots, and we suggest that

a weighted mean $^{206}\text{Pb}/^{238}\text{U}$ age from only the chemically abraded zircon as the best estimate for the age of this sample, i.e., $298.1 \pm 1.1/4.8$ Ma (95% c.l., MSWD = 3.0; Fig. 3D).

5.5.3 Southwestern Aar granite (sample SW1)

From this sample, a total of 28 analyses were carried out, 17 on untreated zircon grains and 11 on zircon grains which were pretreated with an 8 h chemical abrasion. The untreated zircon yielded a more protracted age spectra including younger dates possibly with a slight tendency of younger age from untreated zircon (295.1 ± 3.1 Ma, MSWD = 15.4) compared to 8 h chemically abraded zircon (297.9 ± 3.1 Ma, MSWD = 7.3; Fig. 3D). The high degree of excess scatter is in line with textural indications of pervasive secondary disturbance (Fig. 2) and therefore does not allow for a geologically reasonable calculation of a weighted mean age. The average $^{206}\text{Pb}/^{238}\text{U}$ age of 296 Ma from all 24 analyses is taken as the estimate for the age for this sample.

5.5.4 Garwiidi diorite (sample GD1)

A weighted mean $^{206}\text{Pb}/^{238}\text{U}$ age of $295.6 \pm 2.0/5.8$ Ma (95% c.l., MSWD = 3.4; Fig. 3D) was calculated from 12 analyses of untreated zircon; four normally discordant analyses were not included in this calculation. The large scatter in the spot ages from this sample seems to be in some contrast to undisturbed sector zoning displayed by many zircon grains. However, some analyses touched bright and unzoned rims, which likely formed due to Alpine recrystallization (e.g., analysis Fe16h08).

5.5.5 Aplitic granite (marginal facies of Grimsel granodiorite; sample AR1)

A total of 30 analyses were carried out from this sample, two of which represented xenocrystic zircon at ages of 345 and 465 Ma. Seven analyses were not included in age calculation because they were too old/too young or discordant. The dates of twelve untreated grains and nine grains, which were pretreated with an 8 h chemical abrasion, yielded U–Pb analyses that are overlapping within uncertainty, with a weighted mean of $^{206}\text{Pb}/^{238}\text{U}$ age of 298.6 ± 2.1 Ma (MSWD = 4.4) and 300.0 ± 1.9 Ma (MSWD = 1.9), for the two aliquots respectively. Because of this overlap, we use all analyses to calculate a weighted mean $^{206}\text{Pb}/^{238}\text{U}$ age of $299.2 \pm 1.4/6.8$ Ma (95% c.l., MSWD = 3.7), and interpret that this value reflects the age of crystallization for this sample (Fig. 3D).

5.5.6 Rossbodenstock diorite (sample RD2)

Sixteen of the seventeen analyses of untreated zircon from this sample were tightly overlapping, and

together yield a weighted mean $^{206}\text{Pb}/^{238}\text{U}$ age of $298.6 \pm 1.0/3.6$ Ma (95% c.l., MSWD = 2.2) (Fig. 3D). One analysis was significantly older and therefore was not used for calculation of the mean age.

5.5.7 Tellistock granite (sample T1)

A total of 33 untreated zircon grains were analyzed in two separate analytical sessions (May 2020 and February 2021). The data show a high degree of excess scatter and their mean ages from the two separate sessions are overlapping within internal/analytical uncertainty (297.9 ± 3.2 Ma vs. 303.8 ± 2.3 Ma, respectively; Fig. 3D). After removal of 16 anomalously old, young and/or discordant analyses, a weighted mean $^{206}\text{Pb}/^{238}\text{U}$ age of $301.2 \pm 1.5/5.0$ Ma (95% c.l., MSWD = 2.7) was obtained from 17 analyses.

Finally, two of the samples analyzed yielded excessive scatter within their age spectra, without a reasonable plateau of ages to interpret as reflecting crystallization. Therefore, these two samples are not assigned to one of the above groups, and we do not interpret a U–Pb age from the data presented:

5.5.8 Bristenstock syenite (sample BS1)

No reliable age can be derived from the 16 analyses that scatter between 280 and 445 Ma. Some of the zircon grains exhibit clear core-rim relationships, others show faint and non-planar secondary textures in CL. We interpret this zircon population as heterogeneous in initial crystallization age as well as in the extent of secondary alteration.

5.5.9 Strem granite (sample SG1)

This sample did not yield a robust date, as the 17 analyses show a wide spread of $^{206}\text{Pb}/^{238}\text{U}$ dates from 137 to 597 Ma (Additional file 2: Fig. S19a). The CL imaging revealed abundant xenocrystic core material as well as secondary overprinting (white homogeneous zones, non-planar zones; Fig. 2).

5.6 CA-ID-TIMS U–Pb geochronology (Additional file 4: Table S2)

A total of fifteen grains of the Munt Dado granite (sample MD1) were analyzed by CA-ID-TIMS as a part of this study, and all yielded concordant ages within uncertainty. Fourteen of the ages form a bimodal distribution, with overlapping ages at either 313.8 or 311.8 Ma (Fig. 4A), and one older outlier at an age of 345 Ma. A total of fourteen grains of the Grimsel granodiorite

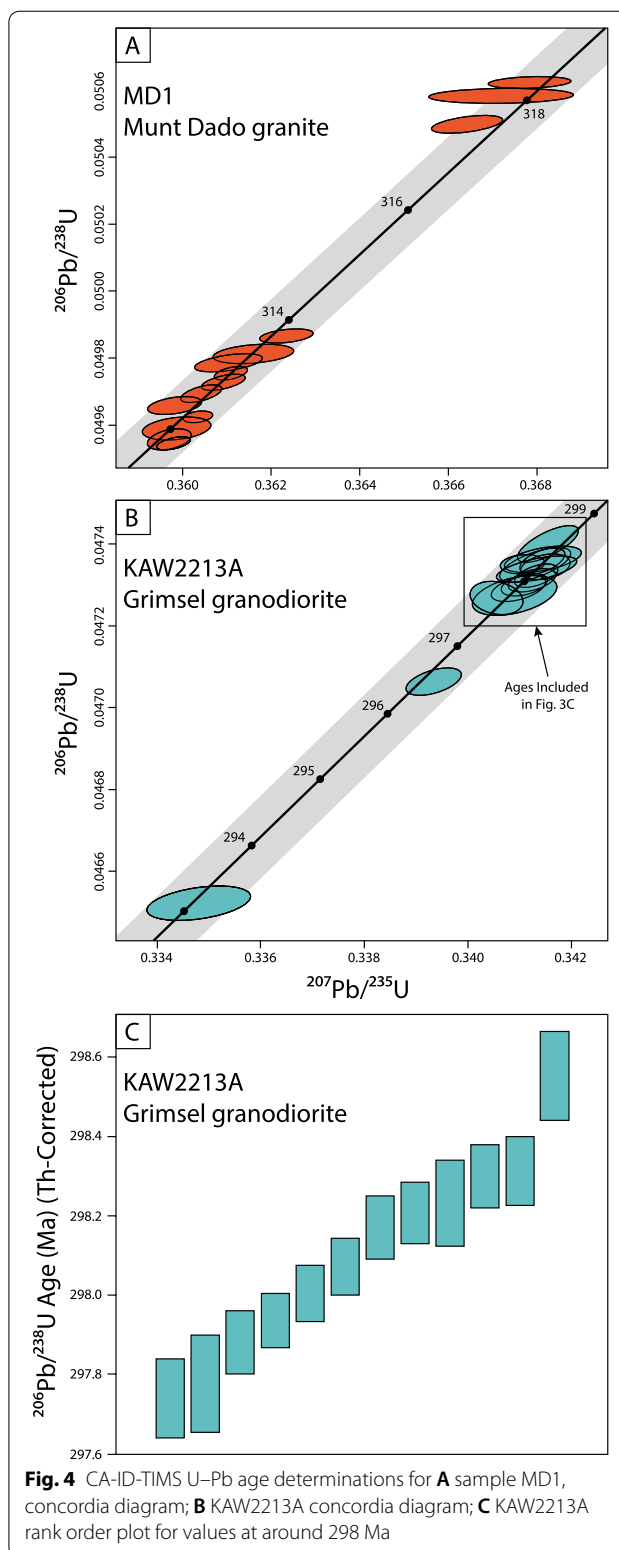
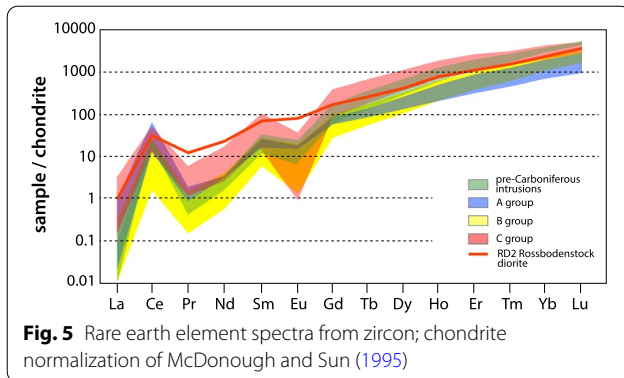


Fig. 4 CA-ID-TIMS U–Pb age determinations for **A** sample MD1, concordia diagram; **B** KAW2213A concordia diagram; **C** KAW2213A rank order plot for values at around 298 Ma

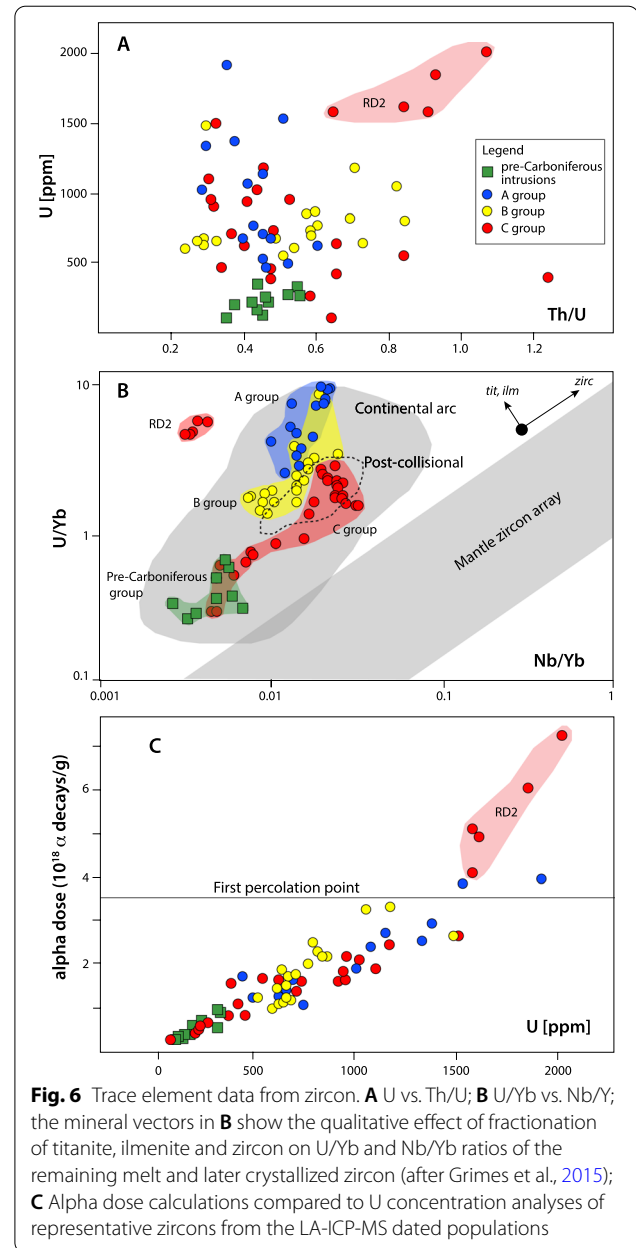


(sample KAW2213A) were analyzed by CA-ID-TIMS as well, and all yielded concordant ages within uncertainty (Fig. 4B). Twelve of the analyses cluster between 297.83 and 298.34 Ma, while two analyses yield anomalously younger ages at 296.6 and 293.2 Ma (Fig. 4C). The twelve dates exhibit significant scatter with an MSWD of 24, and they cannot be considered as a single age population of crystallization.

5.7 Trace elements in zircon (Additional file 5: Table S3)

The full data set of LA-ICP-MS analyses of trace elements is presented in Additional file 5: Table S3; the laser spots for the trace element analyses are indicated in yellow color in the CL images, stored at doi:10.26037/yareta. Among the analyzed trace elements, the only elements that show significant differences between the intrusive units are REE's, U, Th, Nb and Y. The REE patterns in Fig. 5 show the characteristic heavy REE enrichment and the positive Ce anomaly for all four groups of intrusions. Patterns of the pre-Carboniferous intrusions and groups A and B are quite similar, although group B has overall lower LREE's, while group A has lower HREE's. The REE pattern of group C zircon has higher Σ REE and a larger negative Eu-anomaly. Sample RD2 (Rossbodenstock diorite) belongs to age group C but has a distinct pattern with high light REE and no Eu anomaly.

Zircon from the pre-Carboniferous intrusions clearly have the lowest U concentrations, all below 400 ppm, while group A to C zircon mostly scatter between 500 and 2000 ppm U (Fig. 6a). The Th/U ratios of all four groups are between 0.17 and 1.25, with highest values shown by group B and C zircon populations, especially by sample RD2 (Additional file 5: Table S3, Fig. 6a). Figure 6b shows measured U/Yb versus Nb/Y values of zircon compared to the chemical classification of Grimes et al. (2015). The two samples R3 (Russein diorite) and CR2 (Alp Crap Ner tonalite) of pre-Carboniferous intrusions plot into a narrow field at lowest U/Yb of 0.3–0.6. The rest of the analyzed zircon follow a trend of decreasing U/Yb from a



value around 6–8 for Group A (sample KAW676) to 3.2–1.2 for group B, and finally to 5–0.2 for group C, with the lowest U/Yb and Nb/Y values for sample GD1 (Garwiidi diorite). The Rossbodenstock diorite (sample R2) is an exception this trend, as its zircon analyses plot into a distinct field with U/Yb ratios of 4–5 (Fig. 6b) due to high U concentrations, and the lowest Nb/Yb ratios (Additional file 5: Table S3, Fig. 6a).

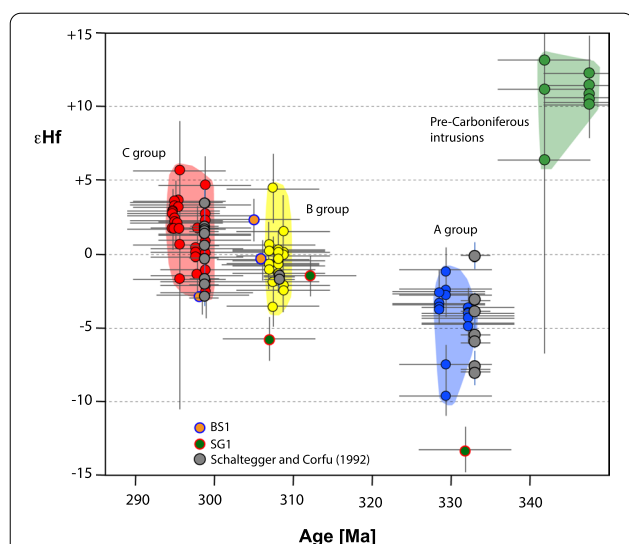


Fig. 7 Initial Hf isotope composition of zircon from the four intrusive pulses of the Aar batholith, determined by LA-MC-ICP-MS. Color coding is identical to Fig. 6a; ϵHf uncertainties are taken from Table F5, age uncertainties represent “extended error”, see the Methods section for more information. Data taken from Schaltegger & Corfu (1992) are in grey; an estimated age error of ± 2 Ma has been adopted.

5.8 Initial Hf isotope composition in zircon (Additional file 7: Table S5)

The results of the Hf isotope analyses are shown in Fig. 7 and presented in Additional file 7: Table S5, and the location of each analysis is shown in blue color on the CL images at doi:10.26037/yareta. Each magmatic pulse yielded largely clustered Hf isotope compositions, without significant outliers within individual pulses. Of the pre-Carboniferous intrusions, sample R3 (Russein diorite) yielded ϵHf values of $+12.3$ to $+10.2$, while three analyses of CR2 did not reproduce well due to low total Hf intensity but yielded similar, however imprecise ϵHf compositions. The hafnium isotope compositions of Group A zircon (samples CM1, PG1, KAW676) range in ϵHf from -1.1 to -9.7 , and the compositions of zircon from Group B (samples KAW3120, AG1, MD1, BG1) are between $+4.4$ and -3.6 . The initial Hf isotopic composition of zircon from Group C (samples KAW2213A, KAW2519, SW1, GD1, AR1, RD2, T1) are very similar to those of Group B, and scatter between $+4.7$ and -2.7 . Our analyses of group A, B and C zircon also overlap within uncertainty with the Hf compositions previously reported by Schaltegger & Corfu (1992) shown as grey dots in Fig. 7. Analyses of zircon from samples BS1 and SG1 are shown separately, they have strongly variable initial ϵHf and U–Pb dates.

6 Discussion of the isotope results

6.1 Interpreting zircon crystallization ages of the Aar batholith

The new U–Pb data, from both LA-ICPMS and ID-TIMS, show significant dispersion in $^{206}\text{Pb}/^{238}\text{U}$ ages. To be able to interpret a crystallization age for a suite of zircon analyses and interpret an emplacement age for the respective igneous lithology, we need to select a sub-population of dates from the age spectrum that may lead to a geologically and statistically valid weighted mean age. In the following we will discuss the potential reasons for the observed scatter. Due to the significant difference in the volume of zircon sampled during a LA-ICPMS analysis relative to the volume analyzed during bulk grain analysis using ID-TIMS, the reason(s) for data scatter may not be identical for the two techniques and need to be assessed separately.

6.2 Interpretation of LA-ICPMS data

All studied zircon samples yielded highly scattered $^{206}\text{Pb}/^{238}\text{U}$ data, despite careful placement of the ablation spots into oscillatory zoned, more marginal domains wherever possible (see spot locations on CL images at doi:10.26037/yareta). The data of most samples contain analyses that are by several percent older or younger than the mean age (Additional file 2: Figs. S3 to S19). In cases where they can be identified as clear outliers, they were not used for the calculation of the mean age. However, in other cases, no such outlier rejection could be reasonably performed due to the lack of a coherent cluster, and therefore we chose not to calculate a weighted mean age. Therefore, from those samples, it is impossible to assess the accurate crystallization age (e.g., samples MD1, BG1, SW1). After this first round of outlier removal, the rest of the data (see $^{206}\text{Pb}/^{238}\text{U}$ age rank order plots of Fig. 3) still do not satisfy the minimum requirements for calculating a statistically significant weighted mean age, since their MSWD values are too high (Wendt & Carl, 1991). Sample R3 is the only exception from this rule (MSWD = 1.4 for $N=18$). The uncertainties based on internal errors (from data scatter only) are in the range of ± 0.3 – 0.7% of the $^{206}\text{Pb}/^{238}\text{U}$ age, which we suspect is optimistic and yields potentially inaccurate uncertainties given the fact that the selection of a data subpopulation was preceded by a subjective outlier rejection and still shows excess scatter. Therefore, as described before, we applied a conservative uncertainty estimate by using half of the difference between the oldest and youngest grain in the selected population of dates. We are confident that the weighted mean LA-ICPMS date of each sample is accurate within these extended error limits. However, given the fact that the mean ages within one single magmatic group seem

to reproduce reasonably well (Fig. 7), we have the feeling that we may overestimate the uncertainty with this conservative approach to error. We consider our selection of dates the best estimate for the age of zircon crystallization, and therefore that these ages approximate the intrusion age of the respective lithology (Table 1).

6.3 Reasons of excess scatter in LA-ICPMS dates

The analyzed igneous zircon populations yield LA-ICPMS zircon data that are very complex. To exclude a systematic bias between U–Pb dates from the LA-ICPMS and ID-TIMS U–Pb geochronology laboratories at the universities of Lausanne and Geneva, the inter-laboratory reproducibility has constantly been verified through paired U–Pb dating in the past (e.g., Chelle-Michou et al., 2014; Schaltegger et al., 2019), and is demonstrated by accurate LA-ICPMS ages from the secondary standard Plešovice as well, which perfectly reproduces the ID-TIMS ages from the Geneva lab (Widmann et al., 2019). Therefore, it is likely that the scatter in this data set is not caused by analytical bias between the two techniques, rather we interpret this difference to be characteristic for this specific sample material. We explore in the following different possible explanations.

6.3.1 Decay damage related Pb-loss

In the case of untreated zircon, LA-ICPMS dates may be variably biased by radiation damage related Pb-loss. According to Murakami et al. (1991), Pb-loss becomes an important process at the second percolation point, equivalent to $8 \cdot 10^{18}$ α -decay events/g, when damaged, aperiodic domains in the zircon lattice become interconnected and radiogenic Pb can migrate within the lattice along fast diffusion pathways. However, this process may also occur at lower α -dose, although maybe not at the same rate. This seems to be the case for most of the analyzed zircon grains in this study: the majority of the zircon crystals analyzed in this study have U concentrations below 1500 ppm (Fig. 5a), equivalent to an α decay dose $< 3.5 \cdot 10^{18}$ a-decay/g given their age of crystallization, and these values are therefore not prone to Pb-loss (Fig. 6c). Zircon from sample RD2 is the only exception to this, which yielded U concentrations consistently above 1,500 ppm. The fact that the reproducibility of 12 h-chemically abraded zircon is better than for non-treated one, e.g., in the case of samples KAW2213A and 2519 (Fig. 3) suggests that a part of age scatter is due to decay-damage related Pb-loss, while most of the scatter requires an explanation that goes beyond unmitigated Pb-loss.

6.3.2 Mixing of growth zones of different age

The presence of different magmatic growth zones close in age in the same zircon is unlikely to be resolved through LA-ICPMS U–Pb dating, because of the high uncertainties associated with single spot analyses. The CL images serve for an optimal placement of the laser spots to particularly avoid obvious inherited cores or younger overgrowths. However, there is little control on zoning along the z-axis, and a zone of slightly different age may be sampled by ablation unintentionally without being distinguishable in the time-resolved concentration scans. The presence of antecrysts from the same magmatic system in a zircon population with slightly different age (e.g., Miller et al., 2007) is of much larger importance in bulk-grain, high-precision ID-TIMS dating.

6.3.3 Presence of pre-intrusive, inherited components

There are a few, anomalously old U–Pb ages within the age spectra in some of the samples, which are interpreted as inherited xenocrystic, inherited cores, which served as nuclei for magmatic precipitation. Since laser spots were intentionally placed into oscillatory zoned marginal regions of zircon, such too old data are scarce in our data set (Additional file 2: Fig. S20). Xenocrystic cores are well visible in CL images of zircon from samples SW1, PG1, BG1, and even more common in BS1 and SG1 (Fig. 2 and images at doi:10.26037/yareta). They may get incorporated from the host rock during magma emplacement (see an example for higher-temperature mafic melts in Gaynor, Svensen, et al., 2022), or alternatively can be entrained in a magma during the melting of igneous or metasedimentary protoliths in the deeper crust, and in this case these cores reflect the anatexic source(s) of the melts (e.g., Miller et al., 2007). The Strem granite (SG1) may be a typical example of an S-type granite issued by (partial) melting of a (meta)sedimentary protolith: it yields a wide range of spot dates up to a $^{206}\text{Pb}/^{238}\text{U}$ spot date of 597 Ma. This would imply high-grade metamorphic conditions at a mid- to lower crustal levels during this late-orogenic magmatic period. On the other hand, young and normally discordant analyses range down to a $^{206}\text{Pb}/^{238}\text{U}$ date of 137 Ma and are likely due to Pb-loss and/or secondary alteration effects (Additional file 3: Table S1). The imprint of the Ordovician-age orogenic cycle (Schaltegger, 1993; Schaltegger et al., 2003) is likely reflected by spot dates between 465 and 430 Ma in samples BS1, SG1, BG1 and AR1 (Table 2), while spot dates of 366–364 Ma in samples R3 and SG1 are more likely the result of mixing volumes of inherited cores and magmatic overgrowth in analysis, rather than a Devonian age component. No Devonian magmatic component has been identified in the Alpine basement to date. There are also some indications that zircon crystals from older and

Table 2 Compilation of previous U–Pb geochronology

Intrusion	Age	U–Pb Method	Reference
Group A/Rötifirn group			
Punteglias and Giuv intrusions	334 ± 2.5 Ma 335.479 ± 0.041/ 0.097/0.37 Ma	Minifractions*, untreated; upper intercept age Single grains, PA and CA	Schaltegger & Corfu (1992) Gaynor, Ruiz, et al. (2022)
Baltschieder granodiorite	336.2 ± 1.7 Ma	Fractions, CA; upper intercept age	Hettmann et al. (2009)
Tödi granite	333 ± 2 Ma	Minifractions, PA	Schaltegger & Corfu (1995)
Group B/Fruttstock group			
Schöllenen syenite	316 ± 27 Ma	Multigrain**, untreated; upper intercept age	Schaltegger & von Quadt (1990)
Düssi diorite	308 ± 2 Ma	Minifractions, PA	Schaltegger & Corfu (1992)
Schöllenen syenite	310 ± 3 Ma	Minifractions, PA	Schaltegger & Corfu (1992)
Voralp granite	309 ± 2 Ma	Minifractions, PA	Schaltegger & Corfu (1992)
Group C/Haslital group			
Central Aar + Mittagflue granites, Grimsel	298 ± 6 Ma	Multigrain, unabraded; upper intercept age	Schaltegger & von Quadt (1990)
Central Aar granites, Reuss valley	296 ± 3 Ma	Multigrain, unabraded; upper intercept age	Schaltegger & von Quadt (1990)
Grimsel granodiorite	299 ± 2 Ma	Minifractions, PA	Schaltegger & Corfu (1992)
Mittagflue granite	296.5 ± 2.5 Ma	Minifractions, PA	Schaltegger & Corfu (1992)
Central Aar granites, Reuss valley	297 ± 2 Ma	Minifractions, PA	Schaltegger & Corfu (1992)
Gastern granite	303 ± 4 Ma	Minifractions, PA	Schaltegger (1993)
Gastern granite	~ 300 Ma	Multigrain***, CA	Hettmann et al. (2009)
Bietschhorn granite	289 ± 3 Ma	Multigrain***, CA; upper intercept age	Hettmann et al. (2009)

CA chemical abrasion, PA physical abrasion

* Minifractions contain ≤ 5 physically abraded grains

** Multigrain fractions consisted of up to 2.5 mg of untreated zircon

*** Multigrain fractions of < 0.05 mg

previously solidified magmatic pulses were integrated into younger melts. For example, the samples CM1 (Group A), and SG1, SW1, MD1 (Group B) contain zircon with spot dates between 345 and 341 Ma, typical for the pre-Carboniferous intrusions. Sample BG1 (Group B) also yields spot dates of 332–330 Ma, typical of Group A dates. Spot dates around 316 Ma in samples BG1 and AR1 (Additional file 3: Table S1) are interpreted to reflect mixing of different age zones.

6.3.4 Secondary replacement of magmatic growth zones

Since the discussed processes cannot explain the ubiquitous excess scatter of the LA-ICPMS dates, we explore here the presence of secondary alteration inside the zircon crystals. The CL images reveal the existence of secondary textures such as (i) non-planar zoned domains that are replacing magmatic oscillatory zones (such as KAW2519, SG1; Fig. 2), and (ii) high-CL zones with irregular shape, sometimes marginal (KAW676) or at sector interfaces, such as intermediate (epitactic) unstructured high-CL zones (SW1), and occasionally around xenocrystic or antecrystic cores (CR2) or around mineral inclusions (KAW2213A). In agreement with the processes described in Geisler et al. (2007), we assume that these are of the effect of dissolution/

reprecipitation and recrystallization processes, respectively. Since they are pervasive inside crystals, and produce low-U recrystallized zircon domains, an analytical bias cannot be mitigated by chemical or physical abrasion. These effects are not reproducible with every studied sample and may possibly be related to the intensity of the microscopically and macroscopically visible Alpine fluid percolation and/or deformation. We, however, have no argument against some of these secondary phenomena being of late Variscan or Permian age (Peverelli et al., 2022).

6.4 Comparing LA-ICP-MS dating of untreated vs. chemically abraded zircon

One of the major goals of this study was the potential improvement of LA-ICPMS U–Pb zircon dating applying chemically abrasion (CA) as a pretreatment, utilizing this pre-treatment for both standard and unknown. The motivation for this experiment is that chemical abrasion pre-treatment has been demonstrated to significantly increase the accuracy of ID-TIMS analyses (e.g., Mattinson, 2005; Widmann et al., 2019). For some samples, zircon material that underwent 4 and 12 h of

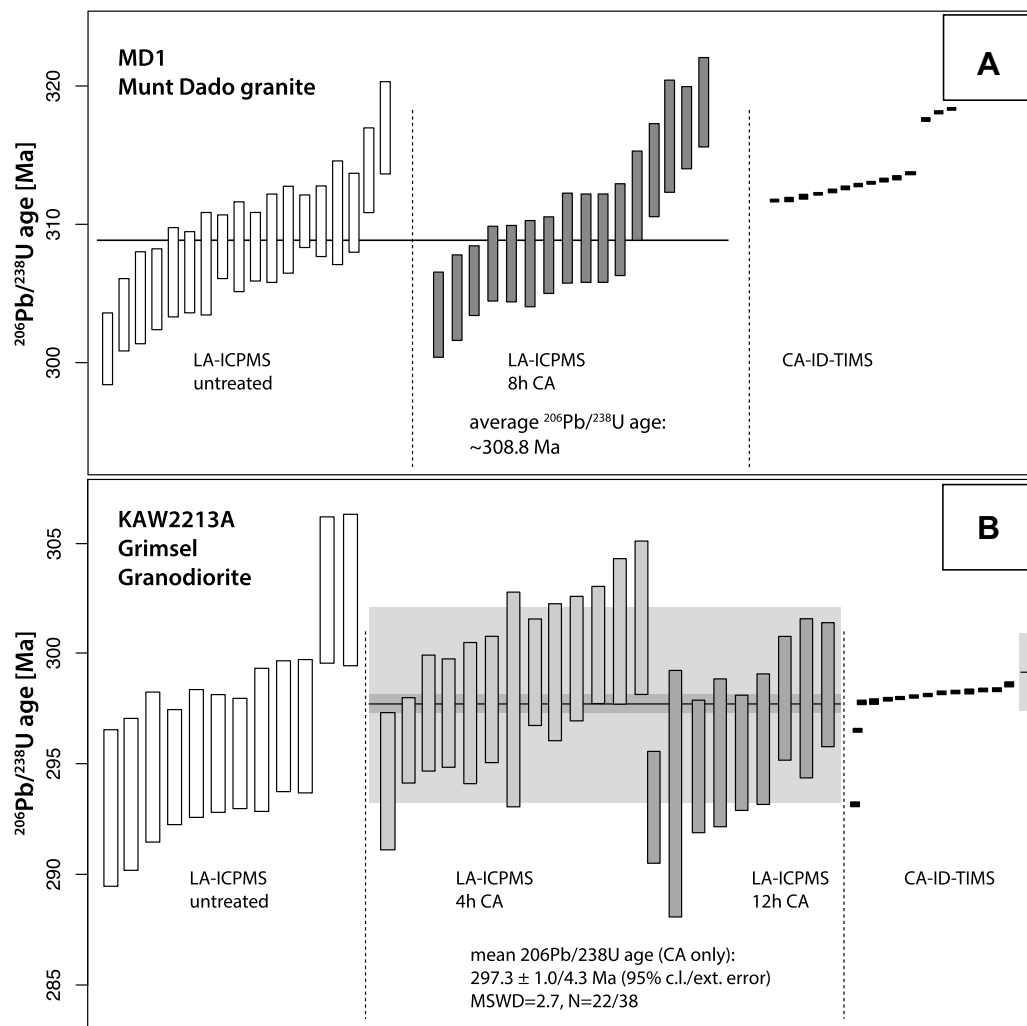


Fig. 8 Comparison of LA-ICPMS ages from both chemically abraded and untreated zircon, with ID-TIMS results from chemically abraded zircon for samples MD1 (A) and KAW2213A (B). ID-TIMS age and estimated uncertainty (grey bar) from Schaltegger & Corfu (1992) is indicated in (B) alongside the new CA-ID-TIMS dates

CA was analyzed separately, for example in the case of KAW2213A and KAW2519 (Fig. 3D). The respective mean dates of the three analyses (untreated, 4 h CA, 12 h CA) do not differ significantly, while, the age spectra from 4 and 12 h chemical abrasion show significantly decreased age dispersion in the case of both samples. The same is, however, not true in other examples, such as in samples MD1 or SW1 (both 8 h CA) because of overall lower quality of the zircon material. The CL images (see lower panel of Fig. 2, and CL images at doi:10.26037/yareta) provide additional evidence of the advantages of using a 12 h chemical abrasion pre-treatment, as specific internal domains were targeted during this partial dissolution step, preferentially removing decay-damaged

zones and non-zircon mineral inclusions (such as apatite) more successfully. Therefore, not only does this approach help to remove crystallographic domains that may have suffered from Pb-loss, but it also removes mineral inclusions which may bias U–Pb ages through the addition of common Pb. The advantages observed in some samples match well with similar observations about CA-LA-ICPMS in other studies (e.g., Crowley et al., 2014; von Quadt et al., 2014). However, chemical abrasion may not be a generally applicable cure for complicated zircon systematics in U–Pb geochronology. In this specific case of the Aar batholith studied here, it does not provide the necessary breakthrough to arrive at more precise and accurate LA-ICPMS age information.

6.5 Interpretation of the CA-ID-TIMS data

Due to the significantly increased precision afforded by CA-ID-TIMS U–Pb geochronology, single zircon data generated with this technique more frequently reveal age dispersion driven by mixing of multiple age domains, including both antecrystic and xenocrystic zircon age domains (e.g., Gaynor, Ruiz, et al., 2022; Schoene et al., 2012). Two samples were analyzed with both LA-ICPMS and CA-ID-TIMS techniques and the data are compared in Fig. 8.

6.5.1 Sample MD1 (*Munt Dado granite*)

The CA-ID-TIMS dates of this sample form two clusters at approximately 318 and between 314–312 Ma (Fig. 4A), while the scattering LA-ICPMS spot dates of the same sample converge at an approximate age of 309 Ma (Figs. 3, 8). The CL images at doi:10.26037/yareta reveal the existence of distinct central portions, rimmed or sometimes truncated by outer oscillatory-zoned growth zones (see example in Fig. 2). The laser spots were preferentially positioned into these latter, more marginal zones. Therefore, by comparing the results (see Fig. 8A) we suggest that the approximate LA-ICPMS date is more accurately reflecting the second, magmatic growth stage relating to pluton formation, while the two age clusters from CA-ID-TIMS reflect mixing of the 309 Ma old age group with some older age component present in the interiors of the zircon crystals.

6.5.2 Sample KAW2213A (*Grimsel granodiorite*)

Another example is given by the scatter of U–Pb CA-ID-TIMS dates of sample KAW2213A (Fig. 4 B,C), showing a main cluster of $^{206}\text{Pb}/^{238}\text{U}$ dates between 297.83 and 298.34 Ma, as well as two distinctly younger analyses. All measurements are analytically concordant (Fig. 4B). Since radioactive decay-damage is below the first percolation point (Fig. 6C), we argue that the age scatter and the two younger dates are not likely due to Pb-loss. This is also corroborated by the fact that 12 h of chemical abrasion had a comparably weak impact on these crystals. Therefore, we favor an interpretation that the age scatter is caused by a mixture between the main volume of Variscan zircon growth and thin rims of later Alpine age zircon growth. The Alpine rims are rather cryptic and cannot be readily recognized in the CL images (see Fig. 2). Our interpretation is supported by the age dispersion and discordance of CA-ID-TIMS dates from zircon of the Punteglias granodiorite in the southeastern part of the Aar massif (sample KAW676, group A; Gaynor, Ruiz, et al., 2022), which yielded clear evidence of the presence of Alpine overgrowths. The laser spot selection for untreated and abraded grains of sample KAW2213A

was mostly successful in avoiding these Alpine rims, the comparison in Fig. 8B thus shows a good coincidence between the results from the two dating techniques.

6.6 How new LA-ICPMS and CA-ID-TIMS U–Pb ages compare to previously published ID-TIMS U–Pb data

The new data together with the data compilation in Table 2 document the analytical development of U–Pb geochronology that has taken place over more than 30 years. The first modern zircon dates of the Aar massif were obtained on milligram fractions of untreated zircon (Schaltegger & von Quadt, 1990), and then progressed to mini-fractions of zircon consisting of <5 physically abraded grains (e.g., Schaltegger & Corfu, 1992, 1995), and to the most recent CA-ID-TIMS analyses of the Aar Massif on single grains (Gaynor, Ruiz, et al., 2022; this study). We present here the first LA-ICPMS U–Pb zircon dates for the Aar massif. Together, these new analyses provide an excellent opportunity to test the potential fidelity of historical geochronology datasets and illustrate the advancements in accuracy and precision.

Our new LA-ICP-MS analyses of untreated zircon from group A samples (CM1: 327.6 ± 1.6 Ma; PG1: 329.9 ± 1.9 Ma; Table 1) yield slightly younger dates than the age of 336.2 ± 1.7 Ma for the Baltschieder granite (western Aar massif) in Hettmann et al. (2009), as well as the pooled age of 334 ± 2.5 Ma in Schaltegger and Corfu (1992) for the Giuv syenite and Punteglias granite in the eastern Aar massif (Table 2). In the latter case, they agree within the extended errors of ± 3.8 and 5.2 Ma, respectively, underlining the importance of correct error assessment in LA-ICPMS dating. The accuracy of the bulk grain ID-TIMS, upper intercept age of 334 ± 2.5 Ma in Schaltegger & Corfu (1992) for the Punteglias granite was confirmed by a single-grain PA-CA-ID-TIMS weighted mean $^{206}\text{Pb}/^{238}\text{U}$ age of $335.479 \pm 0.041/0.097/0.37$ Ma of Gaynor, Ruiz, et al. (2022); Table 2). A similar relationship also exists for group B intrusions, comparing our dates of $307.1 \pm 1.6/5.3$ Ma (KAW3120) and $307.4 \pm 2.0/4.4$ Ma (AG1) as well as the approximate age estimates of 308.8 Ma (MD1) and 311 Ma (BG1) overlap within uncertainty with the ages between 308 ± 2 and 310 ± 3 Ma from Schaltegger & Corfu (1992) for these rocks. The same holds for the group C intrusive rocks (KAW2213 and 2519, SW1, GD1, AR1, RD2, T1), where LA-ICPMS U–Pb ages from zircon from all samples yield a narrow age range between $295.6 \pm 2.0/5.8$ Ma (GD1) and $301.2 \pm 1.5/5.0$ Ma (T1). The coincidence is best highlighted by the comparison of the available ages for the granodiorites of Grimsel (KAW2213A) and Reuss valley (KAW2519): Our new CA-LA-ICPMS

dates of 297.2 ± 1.0 and 298.1 ± 1.1 Ma, as well as the CA-ID-TIMS dates for KAW2213A between 297.83 and 298.34 Ma are in perfect coincidence with the dates in Schaltegger & Corfu (1992) of 299 ± 2 Ma (for sample KAW2213A; Fig. 8B) and 297 ± 2 Ma for Reuss valley granites, among them sample KAW2519 (Table 2), and also agree with upper intercept ages of 298 ± 6 and 296 ± 3 Ma of Schaltegger & Quadt (1990) obtained on non-treated milligram-sized multigrain fractions.

6.7 How do the new Hf isotope analyses compare to previously published values

The only available data set was published by Schaltegger & Corfu (1992) using 0.5–2.5 mg zircon fractions and ID-TIMS techniques. The initial Hf isotope data from this study are shown in Fig. 7 as grey symbols and demonstrate the excellent reproducibility with our new LA-ICPMS data. The fact that mg-fractions of zircon yield identical ϵ_{Hf} with laser spot analyses suggest that these zircons are relatively homogeneous in initial Hf isotopic composition.

7 Implications for the magmatic evolution at the end of the Variscan orogeny in the Aar massif

The intrusive rocks studied in this paper document the approximately 50 myr long evolution of magmatism in the Aar batholith during a late stage of the Variscan orogeny. For reconstruction of the source of the magmas, we combine trace element compositions of zircon, the presence of inherited components in dated zircon crystals, and the Hf isotope compositions of these grains. A pulsed assembly of the Aar batholith was previously suggested by Schaltegger and Corfu (1992, 1995), and further developed in Schaltegger (1997). New U–Pb zircon geochronology of this study as well as of Gaynor, Ruiz, et al. (2022) corroborates the existence of three previously proposed magmatic pulses at approximately 333, 309 and 298 Ma (Fig. 7), and also assigns an age to several smaller intrusions which were not previously dated. In addition to these three pulses, two intrusions from the southeastern end of the Aar massif (Russein diorite R3, and Alp Crap Ner tonalite CR2) yielded older ages, so we propose these intrusions reflect an earlier generation of pre-Carboniferous intrusions within the batholith, and call this the “Surselva Group” (Table 1; Fig. 1). The new U–Pb ages are essential for the correct presentation of Variscan magmatic rocks on the new Aar massif map sheets of the Geological Atlas of Switzerland. Several of the dated lithologies represent smaller intrusive bodies, marginal to the most voluminous Central Aar granite intrusion (group C) and usually strongly sheared and altered. The Alpine deformation obliterated all magmatic

contacts, which makes assessment of relative age relations between different intrusions in the field impossible, leaving U–Pb dating the only possibility to correlate these with the observed four magmatic pulses.

The trace elements in zircon of the Aar batholith are typical compositions observed in continental arc magmatism, with elevated U/Yb and low Nb/Yb ratios (Grimes et al., 2015; Fig. 6B). Zircon from the pre-Carboniferous intrusions (samples R3 and CR2) plot at lowest U concentrations and lowest U/Yb ratios, and have a Hf isotopic composition ($\epsilon_{\text{Hf}} = +10 - +12$), close to that of the depleted mantle at the time of crystallization (ϵ_{Hf} of approximately +15.5). This pulse may have formed in an Andean-type continental arc scenario, associated with subduction consuming the Rhenohercynian oceanic crust at the continental margin of the Variscan terrane collage. This tectonic event was first suggested by von Raumer et al. (2013), however not previously identified in the igneous record of the Aar batholith. The significantly more radiogenic Hf isotopic composition of these approximately 348 Ma intrusions is indicative of a significant incorporation of a depleted mantle component, which has also been observed in the coeval rocks exposed in the Massif Central (Vanderhaeghe et al., 2020). This differs from the coeval rocks of the Bohemian Massif, which instead likely incorporated a larger crustal component in their magma genesis, based on whole-rock Sr, and Nd isotopes (Janoušek et al., 2000).

The continental margin stage at approximately 348 Ma was followed by collision and subduction of the Saxothuringian domain below the Moldanubian domain, and eventually extension of the overthickened lithosphere in the post-collisional stage (e.g., Schulmann et al., 2014; von Raumer et al., 2013). The timing of the emplacement of group A, B to C intrusions of the Aar batholith therefore needs to be integrated into this overall geodynamic scenario. There is a clear temporal trend from A to B to C groups with decreasing U/Yb at constant Nb/Yb (Fig. 6B) and increasing ϵ_{Hf} values in zircon (Fig. 7), pointing to a temporal evolution of magma compositions in this geodynamic context, involving different, mantle and crustal source components. The approximately 333 Ma old group A rocks are part of the high-K magmatic suite, also termed “durbachites”, which are present in most of the Variscan orogen (see compilation in von Raumer et al., 2014; or, e.g., Janoušek et al., 2020; Kotková et al., 2010, for the Bohemian Massif; Vanderhaeghe et al., 2020, for the Massif Central; Tabaud et al., 2015, for the Vosges, among many others). They have been interpreted as products of large-scale partial melting, affected strongly by enriched lithospheric mantle and lower crustal domains within the extending orogenic root (e.g., Schulmann et al., 2014; Vanderhaeghe et al., 2020). These rocks incorporated a

distinct crustal component during their magma genesis, which is reflected by low ϵ_{Hf} compositions down to -9 (Fig. 7) and elevated U/Yb abundance ratios (Fig. 6b). Either of these compositions could have formed due to melting of significantly enriched lithospheric mantle and/or by direct assimilation of crust. This component decreases in importance from A through B to C groups (Fig. 6B), possibly as a function of progressive melt depletion during the late-orogenic thinning and decompression of the lithosphere (Schaltegger, 1997), and increasing influence of melt advection and/or remelting of more depleted mantle sources (see Schaltegger & Corfu, 1992).

The group C intrusions may therefore represent magmas formed with the highest relative proportion of juvenile mantle, due to ϵ_{Hf} values up to $+5.5$, and lowest U/Yb values similar to the subduction-stage magmatism (Fig. 6B). However, the two element ratios (U/Yb, Nb/Yb) do not unequivocally distinguish between the magma source and fractionation effects during magmatic evolution; zircon fractionation would lead to positively correlated trends towards higher U/Yb and Nb/Yb in the remaining magma and successively crystallizing zircon, whereas titanite and ilmenite removal will decrease the Nb/Yb but increase the U/Yb of the liquid (see qualitative fractionation trends indicated in Fig. 6B). Therefore, the positive trend of increasing U/Yb and Nb/Yb displayed by zircon from group C intrusions is mainly due to fractionation of zircon. The zircon analyses from diorite RD2 plot into a distinctly separate field at high U/Yb (Fig. 6B), due to very high U concentrations (Additional file 5: Table S3, Fig. 6B), and therefore may relate to late saturation of zircon in a U-rich residual melt after extensive fractionation of U-poor mafic minerals.

8 Conclusions

1. The magmatic zircon crystals of the Aar batholith studied here exhibit multiple forms of complexity, including inheritance, domains of Alpine secondary alteration or growth, decay damage related lead loss, and possibly protracted magmatic growth. These complexities lead to excess scatter within the individual LA-ICPMS and CA-ID-TIMS U–Pb data sets. These different components of potential error are variably present in the data, and their expression within age spectra is variable based upon which pre-treatment method and analytical technique were used. We can exclude analytical fluctuations being the cause for the observed scatter, via the very reproducible datasets from the primary standard (GJ-1 reference zircon) and the secondary standard (Plešovice reference zircon) for the LA-ICPMS analyses and the reproducibility of the ET100 synthetic solution for the ID-TIMS analyses.
2. Decay-damage related Pb-loss is a subordinate source of age scatter, which can be reduced by 12 h chemical abrasion prior to analysis by LA-ICPMS techniques to some extent. However, due to other complications present within the zircon studied here, it is not capable of completely mitigating the scatter present in this data set.
3. After rejection of obvious outliers and normally discordant points, the remaining data still exhibit substantial excess scatter with MSWD values outside the acceptable limits for statistically equivalent data populations. Weighted mean $^{206}\text{Pb}/^{238}\text{U}$ dates with 0.3–0.7% uncertainties at 95% confidence level, calculated from data scatter alone, are potentially inaccurate.
4. With new LA-ICPMS dates, we were able to reproduce the three known magmatic pulses of the Aar batholith at approximately 333 Ma for the Group A/Rötifirn group, 309 Ma for the group B/Fruttstock group, and 298 Ma for the group C/Haslital group. In addition, we identify a pulse of pre-Carboniferous intrusions at ca. 348 Ma we term “Surselva group”. This older pulse is likely derived from melting of depleted mantle, and we interpret this pulse as a relic of active continental arc magmatism. It is followed by the three pulses of late-orogenic extensional to transtensional magmatism: The 333 Ma melts are derived from metasomatically enriched lithospheric mantle, possibly contaminated by crustal melts, while the following pulses at 309 and 298 Ma incorporate an increasing component of juvenile mantle sources present in the magmas. This geodynamic scenario is reflected by an increase of initial ϵ_{Hf} values from -8 at ~ 333 Ma to $+5$ at ~ 298 Ma.
5. The new U–Pb ages are essential for the correct presentation of Variscan magmatic rocks on the new Aar massif map sheets of the Geological Atlas of Switzerland and allow for assignment of hitherto undated intrusions to one of the four magmatic pulses. Ubiquitous Alpine deformation obliterated many of the magmatic contacts, which together with partly challenging outcrop conditions may render an assessment of relative age relations between different intrusions in the field very difficult.

Supplementary Information

The online version contains supplementary material available at <https://doi.org/10.1186/s00015-022-00420-1>.

Additional file 1. Characterization of the zircon growth textures revealed by CL imaging.

Additional file 2: Fig. S1. LA-ICP-MS data for primary standard JG-1, (A) untreated, (B) chemically abraded. **Fig. S2.** LA-ICP-MS data for secondary standard Plesovice, (A) untreated, (B) chemically abraded. **Fig. S3.** LA-ICP-MS data for sample R3 (Russein diorite); a) 206Pb/238U age scatter plot; b) Concordia diagram. **Fig. S4.** LA-ICP-MS data for sample CR2 (Alp Crap Ner tonalite); a) 206Pb/238U age scatter plot; b) Concordia diagram. **Fig. S5.** LA-ICP-MS data for sample CM1 (Curtin monzonite); a) 206Pb/238U age scatter plot; b) Concordia diagram. **Fig. S6.** LA-ICP-MS data for sample PG1 (Pardatschas granite); a) 206Pb/238U age scatter plot; b) Concordia diagram. **Fig. S7.** LA-ICP-MS data for sample KAW3120 (Düssi diorite); a) 206Pb/238U age scatter plot; b) Concordia diagram. **Fig. S8.** LA-ICP-MS data for sample AG1 (Leucocratic aplitic granite, Grueben glacier); a) 206Pb/238U age scatter plot; b) Concordia diagram. **Fig. S9.** LA-ICP-MS data for sample MD1 (Munt Dado granite); a) 206Pb/238U age scatter plot; b) Concordia diagram. **Fig. S10.** LA-ICP-MS data for sample BG1 (Bugnei granodiorite); a) 206Pb/238U age scatter plot; b) Concordia diagram. **Fig. S11.** LA-ICP-MS data for sample KAW2213A (Grimsel granodiorite); a) 206Pb/238U age scatter plot; b) Concordia diagram. **Fig. S12.** LA-ICP-MS data for sample KAW2519 (Reuss granodiorite); a) 206Pb/238U age scatter plot; b) Concordia diagram. **Fig. S13.** LA-ICP-MS data for sample SW1 (Southwestern Aar granite); a) 206Pb/238U age scatter plot; b) Concordia diagram. **Fig. S14.** LA-ICP-MS data for sample GD1 (Garwiidi diorite); a) 206Pb/238U age scatter plot; b) Concordia diagram. **Fig. S15.** LA-ICP-MS data for sample AR1 (Aplitic granite, marginal facies of the Grimsel granodiorite); a) 206Pb/238U age scatter plot; b) Concordia diagram. **Fig. S16.** LA-ICP-MS data for sample RD2 (Rossbodenstock diorite); a) 206Pb/238U age scatter plot; b) Concordia diagram. **Fig. S17.** LA-ICP-MS data for sample T1 (Tellistock granite); a) 206Pb/238U age scatter plot; b) Concordia diagram. **Fig. S18.** LA-ICP-MS data for sample BS1 (Bristenstock syenite); a) 206Pb/238U age scatter plot; b) Concordia diagram. **Fig. S19.** LA-ICP-MS data for sample SG1 (Strem granite), concordia diagram. **Fig. S20.** Kernel density estimate (KDE) of all LA-ICPMS spot ages obtained in this study.

Additional file 3: Table S1. Results of U-Pb age determinations by LA-ICP-MS; a) unknowns; b) GJ-1 reference zircon (primary standard); c) Plesovice reference zircon (secondary standard)

Additional file 4: Table S2. Results of U-Pb age determinations by CA-ID-TIMS.

Additional file 5: Table S3. Trace element analyses by LA-ICP-MS

Additional file 6: Table S4. Repeatability of LA-ICPMS measurements of trace elements on zircon reference material GJ-1.

Additional file 7: Table S5. Hf isotope analyses by LA-MC-ICP-MS.

Acknowledgements

We are extremely thankful for the help of A. Ulianov during the process of collecting and treating the U-Pb age data at University of Lausanne. Technical help of J.M. Boccard for preparation of the epoxy resin zircon mounts, and of A. Martignier for CL imaging is gratefully acknowledged. The Swiss National Science Foundation is thanked for its longstanding support of the research infrastructure at universities of Geneva and Lausanne. The presented study benefited from financial support by the Swiss Geological Survey (Federal Office of Topography of Switzerland swisstopo). We acknowledge and highly appreciate two detailed anonymous reviews, which clarified, completed and rectified many points.

Author contributions

MR: sample preparation and mineral separation, data acquisition, writing; US: project design, writing, data compilation and figures; SPG: sample preparation, chemical abrasion, CA-ID-TIMS data acquisition, data compilation, editing; MC: Hf isotope data acquisition, editing; JA: sampling, editing; CG: sampling, editing; FG: sampling, editing; MW: project design, sampling, editing. All authors read and approved the final manuscript.

Funding

This study was funded by a grant from swisstopo in the frame of the preparation of map sheets of the Geological Atlas of Switzerland 1:25'000.

Availability of data and materials

Analytical data (U-Pb, Hf isotopes, trace elements analyses) are available in the Additional files. CL images of all dated zircon crystals are available at doi:10.26037/yareta.

Declarations

Ethics approval and consent to participate

Not applicable

Consent for publication

Not applicable

Competing interests

The authors declare no competing interests.

Author details

¹Département des Sciences de la Terre, Université de Genève, rue des Maraichers 13, 1205 Geneva, Switzerland. ²Dahlienweg 5, Jegenstorf, Switzerland. ³Kellerhals + Haefeli AG, Lucerne, Switzerland. ⁴CSD Ingenieure AG, Thuisis, Switzerland. ⁵Swiss Geological Survey, Federal Office of Topography Swisstopo, Wabern, Switzerland.

Received: 16 March 2022 Accepted: 28 May 2022

Published online: 18 July 2022

References

- Abrecht, J. (2022). Blatt 1230 Guttannen. Geol. Atlas Schweiz 1:25000, explanatory notes, 174
- Albarede, F., Telouk, P., Blichert-Toft, J., Boyet, M., Agranier, A., & Nelson, B. (2004). Precise and accurate isotopic measurements using multiple-collector ICPMS. *Geochimica Et Cosmochimica Acta*, 68(12), 2725–2744. <https://doi.org/10.1016/j.gca.2003.11.024>
- Allen, C. M., & Campbell, I. A. (2012). Identification and elimination of a matrix-induced systemic error in LA-ICP-MS ²⁰⁶Pb/²³⁸U dating of zircon. *Chemical Geology*, 332–333, 157–165.
- Balleve, M., Manzotti, P., & Piazz, G. V. D. (2018). Pre-alpine (Variscan) inheritance: a key for the location of the future Valais Basin (Western Alps). *Tectonics*, 37, 786–817. <https://doi.org/10.1002/2017TC004633>
- Berger, A., Mercolli, I., Herwegh, M., & Gnos, E. (2016). Geological map of the Aar Massif, Tavetsch and Gotthard Nappes. *Geological special Map 1:100000, map sheet 129*.
- Berger, A., Mercolli, I., Herwegh, M., & Gnos, E. (2017). Geological map of the Aar Massif, Tavetsch and Gotthard Nappes. *Geological special Map 1:100000, explanatory notes*, 129.
- Boekhout, F., Spikings, R., Sempere, T., Chiaradia, M., Ulianov, A., & Schaltegger, U. (2012). Jurassic arc magmatism along the southern Peruvian margin during Pangea breakup and dispersal. *Lithos*, 146–147, 48–64. <https://doi.org/10.1016/j.lithos.2012.04.015>
- Bouvier, A., Vervoort, J., & Patchett, P. (2008). The Lu-Hf and Sm-Nd isotopic composition of CHUR: Constraints from unequilibrated chondrites and implications for the bulk composition of terrestrial planets. *Earth and Planetary Science Letters*, 273(1–2), 48–57. <https://doi.org/10.1016/j.epsl.2008.06.010>
- Bowring, J. F., McLean, N. M., & Bowring, S. A. (2011). Engineering cyber infrastructure for U-Pb geochronology: Tripoli and U-Pb_Redux. *Geochronology, Geophysics, Geosystems*. <https://doi.org/10.1029/2010GC003479>
- Bussy, F., Hernandez, J., & von Raumer, J. (2000). Bimodal magmatism as a consequence of the post-collisional readjustment of the thickened Variscan continental lithosphere (Aiguilles Rouges/Mont-Blanc Massifs, western Alps). *Transactions of the Royal Society of Edinburgh-Earth Sciences*, 91, 221–233. <https://doi.org/10.1017/S0263593300007392>
- Chelle-Michou, C., Chiaradia, M., Ovtcharova, M., Ulianov, A., & Wotzlaw, J.-F. (2014). Zircon petrochronology reveals the temporal link between porphyry systems and the magmatic evolution of their hidden plutonic roots (the Eocene Corocochuayco deposit, Peru). *Lithos*, 198–199(C), 129–140.
- Condon, D. J., Schoene, B., McLean, N. M., Bowring, S. A., & Parrish, R. R. (2015). Metrology and traceability of U-Pb isotope dilution geochronology

- (EARTHTIME Tracer Calibration Part I). *Geochimica Et Cosmochimica Acta*, 164, 464–480. <https://doi.org/10.1016/j.gca.2015.05.026>
- Conte, A. M., Cuccurru, S., D'Antonio, M., Naitza, S., Oggiano, G., & Secchi, F. (2017). The post-collisional late Variscan ferroan granites of southern Sardinia (Italy): Inferences for inhomogeneity of lower crust. *Lithos*, 294–295, 263–282. <https://doi.org/10.1016/j.lithos.2017.09.028>
- Crowley, Q., Heron, K., Riggs, N., Kamber, B., Chew, D., McConnell, B., & Benn, K. (2014). Chemical abrasion applied to LA-ICP-MS U–Pb zircon geochronology. *Minerals*, 4(2), 503–518. <https://doi.org/10.3390/min4020503>
- Fisher, C. M., Vervoort, J. D., & DuFrane, S. A. (2014). Accurate Hf isotope determinations of complex zircons using the “laser ablation split stream” method. *Geochemistry, Geophysics, Geosystems*, 15(1), 121–139. <https://doi.org/10.1002/2013GC004962>
- Gaynor, S. P., Ruiz, M., & Schaltegger, U. (2022). Evaluating U–Pb geochronology: How method selection and its precision impacts scientific interpretation of age spectra. *Chemical Geology*, 15, 120913. <https://doi.org/10.1016/j.chemgeo.2022.120913>
- Gaynor, S. P., Svensen, H., Polteau, S., & Schaltegger, U. (2022). Local melt contamination and global climate impacts: Dating the emplacement of Karoo LIP sills in organic-rich shale. *Earth and Planetary Science Letters*, 579, 117371. <https://doi.org/10.1016/j.epsl.2022.117371>
- Geisler, Th., Schaltegger, U., & Tomaschek, F. (2007). Re-equilibration of zircon in aqueous fluids and melts. *Elements*, 3, 44–50.
- Gisler, C. (2018). Blatt 1212 Amsteg. *Geological Atlas Schweiz 1:25000, explanatory notes*, 160.
- Gisler, C., Labhart, T., Spillmann, P., Herwegh, M., Della Valle, G., Trüssel, M., & Wiederkehr, M. (2020). Blatt 1210 Innertkirchen. *Geological Atlas Schweiz 1:25000, explanatory notes*, 167.
- Grimes, C. B., Wooden, J. L., Cheadle, M., & John, B. E. (2015). “Fingerprinting” tectono-magmatic provenance using trace elements in igneous zircon. *Contributions to Mineralogy and Petrology*, 170(5), 1–26. <https://doi.org/10.1007/s00410-015-1199-3>
- Grünenfelder, M. (1963). Heterogenität akzessorischer Zirkone und die petrogenetische Deutung ihrer Uran/Blei-Zerfallsalter: I. Der Zirkon des Granodioritgneises von Acquacalda. *Schweizerische Mineralogische und Petrographische Mitteilungen*, 43, 23 p.
- Guillot, S., & Ménot, R. (2009). Paleozoic evolution of the external crystalline massifs of the Western Alps. *Comptes Rendus-Géoscience*, 341, 253–265. <https://doi.org/10.1016/j.crte.2008.11.010>
- Hettmann, K., Siebel, W., Spiegel, C., & Reinecker, J. (2009). Granite genesis and migmatization in the western Aar Massif Switzerland. *Neues Jahrbuch Für Mineralogie-Abhandlungen*, 186(3), 309–320. <https://doi.org/10.1127/0077-7757/2009/0150>
- Hiess, J., Condon, D. J., McLean, N., & Noble, S. (2012). 238U/235U systematics in terrestrial uranium-bearing minerals. *Science*, 335(6076), 1610–1614.
- Hora, J. M., Tabaud, A.-S., Janoušek, V., & Kochergina, Y. V. E. (2021). Potassic magmas of the Vosges Mts (NE France) delimit the areal extent and nature of long-gone Variscan orogenic mantle domains. *Lithos*, 402–403, 106304. <https://doi.org/10.1016/j.lithos.2021.106304>
- Horstwood, M. S. A., Košler, J., Gehrels, G., Jackson, S. E., McLean, N. M., Paton, C., Pearson, N. J., Sircombe, K., Sylvester, P., Vermeesch, P., Bowring, J. F., Condon, D. J., & Schoene, B. (2016). Community-derived standards for LA-ICP-MS U-(Th)-Pb geochronology—uncertainty propagation, age interpretation and data reporting. *Geostandards and Geoanalytical Research*, 40(3), 311–332. <https://doi.org/10.1111/j.1751-908X.2016.00379.x>
- Janoušek, V., Bowes, D. R., Rogers, G., Farrow, C. M., & Jelinek, E. (2000). Modeling diverse processes in the petrogenesis of a composite batholith: The Central Bohemian Pluton, Central European Hercynides. *Journal of Petrology*, 41(4), 511–543.
- Janoušek, V., Hanžl, P., Svojtka, M., Hora, J. M., Kochergina, Y. V. E., Gadas, P., Holub, F. V., Gerdes, A., Verner, K., Hrdličková, K., Daly, J. S., & Buriánek, D. (2020). Ultrapotassic magmatism in the heyday of the Variscan Orogeny: The story of the Třebíč Pluton, the largest durbachitic body in the Bohemian Massif. *International Journal of Earth Sciences*, 109(5), 1–44. <https://doi.org/10.1007/s00531-020-01872-2>
- Klötzli, U., Klötzli, E., Günes, Z., & Kosler, J. (2009). Accuracy of laser ablation U–Pb zircon dating: Results from a test using five different reference zircons. *Geostandards and Geoanalytical Research*, 33(1), 5–15.
- Kotková, J., Schaltegger, U., & Leichmann, J. (2010). Two types of ultrapotassic plutonic rocks in the Bohemian Massif—coeval intrusions at different crustal levels. *Lithos*, 115, 163–217. <https://doi.org/10.1016/j.lithos.2009.11.016>
- Mattinson, J. (2005). Zircon U–Pb chemical abrasion (“CA-TIMS”) method: Combined annealing and multi-step partial dissolution analysis for improved precision and accuracy of zircon ages. *Chemical Geology*, 220(1–2), 47–66. <https://doi.org/10.1016/j.chemgeo.2005.03.011>
- McDonough, W. F., & Sun, S. S. (1995). The composition of the earth. *Chemical Geology*, 120, 223–253.
- McLean, N. M., Bowring, J. F., & Bowring, S. A. (2011). An algorithm for U–Pb isotope dilution data reduction and uncertainty propagation. *Geochemistry, Geophysics, Geosystems*, 12(6), Q0AA18. <https://doi.org/10.1029/2010GC003478>
- McLean, N. M., Condon, D. J., Schoene, B., & Bowring, S. A. (2015). Evaluating uncertainties in the calibration of isotopic reference materials and multi-element isotopic tracers (EARTHTIME Tracer Calibration Part II). *Geochimica Et Cosmochimica Acta*, 164, 481–501. <https://doi.org/10.1016/j.gca.2015.02.040>
- Miller, J., Matzel, J., Miller, C., Burgess, S., & Miller, R. (2007). Zircon growth and recycling during the assembly of large, composite arc plutons. *Journal of Volcanology and Geothermal Research*, 167(1–4), 282–299. <https://doi.org/10.1016/j.volgeores.2007.04.019>
- Morel, M. L. A., Nebel, O., Nebel-Jacobsen, Y. J., Miller, J. S., & Vroon, P. Z. (2008). Hafnium isotope characterization of the GJ-1 zircon reference material by solution and laser-ablation MC-ICPMS. *Chemical Geology*, 255(1–2), 231–235. <https://doi.org/10.1016/j.chemgeo.2008.06.040>
- Mundil, R., Ludwig, K. R., Metcalfe, I., & Renne, P. R. (2004). Age and timing of the Permian mass extinctions: U/Pb dating of closed-system zircons. *Science*, 305(5691), 1760–1763.
- Murakami, T., Chakoumakos, B. C., Ewing, R. C., Lumpkin, G. R., & Weber, W. J. (1991). Alpha-decay event damage in zircon. *American Mineralogist*, 76(9–10), 1510–1532.
- Patchett, P. J., & Tatsumoto, M. (1980). Hafnium isotope variations in oceanic basalts. *Geophysical Research Letters*, 7(12), 1077–1080.
- Peverelli, M., Berger, A., Mulch, A., Pettke, T., Piccoli, F., & Herwegh, M. (2022). Epidote U–Pb geochronology and H isotope geochemistry trace pre-orogenic hydration of mid-crustal granitoids. *Geology*, in press. <https://doi.org/10.1130/G50028.1>
- von Quadt, A., Gallhofer, D., Guillon, M., Peytcheva, I., Waelle, M., & Sakata, S. (2014). U–Pb dating of CA/non-CA treated zircons obtained by LA-ICP-MS and CA-TIMS techniques: Impact for their geological interpretation. *Journal of Analytical Atomic Spectrometry*, 29(9), 1618–1629.
- von Raumer, J. F., Bussy, F., Schaltegger, U., Schulz, B., & Stampfli, G. M. (2013). Pre-Mesozoic Alpine basements—their place in the European Paleozoic framework. *Geological Society of America Bulletin*, 125(1–2), 89–108. <https://doi.org/10.1130/B30654.1>
- von Raumer, J. F., Finger, F., Veselá, P., & Stampfli, G. M. (2014). Durbachites-Vaugnerites—a geodynamic marker in the central European Variscan orogen. *Terra Nova*, 26, 85–95. <https://doi.org/10.1111/ter.12071>
- Rosera, J. M., Gaynor, S. P., & Coleman, D. S. (2021). Spatio-temporal shifts in magmatism and mineralization in Northern Colorado beginning in the late Eocene. *Economic Geology*, 116(987–1), 010.
- Schaltegger, U. (1990). The Central Aar Granite: Highly differentiated calc-alkaline magmatism in the Aar Massif, Central Alps, Switzerland. *European Journal of Mineralogy*, 2, 245–259.
- Schaltegger, U., & von Quadt, A. (1990). U–Pb zircon dating of the Central Aar Granite (Aar Massif, Switzerland). *Schweizerische Mineralogisch-Petrographische Mitteilungen*, 70, 361–371.
- Schaltegger, U. (1994). Unravelling the Pre-Mesozoic history of Aar and Gotthard massifs (Central Alps, Switzerland) by isotopic dating—a review. *Schweizerische Mineralogisch-Petrographische Mitteilungen*, 74, 37–47.
- Schaltegger, U., Abrecht, J., & Corfu, F. (2003). An Ordovician orogeny in the Alpine basement: constraints from geochronology and geochemistry (Aar massif, Central Alps). *Schweizerische Mineralogisch-Petrographische Mitteilungen*, 83, 183–195.
- Schaltegger, U. (1993). The evolution of the polymetamorphic basement of the Central Alps unravelled by precise U–Pb zircon dating. *Contributions to Mineralogy and Petrology*, 113, 466–478.
- Schaltegger, U. (1997). Magma pulses in the Central Variscan Belt: Episodic melt generation and emplacement during lithospheric thinning. *Terra Nova*, 9(5–6), 242–245.

- Schaltegger, U., & Corfu, F. (1992). The age and source of late Hercynian magmatism in the central Alps: Evidence from precise U–Pb ages and initial Hf isotopes. *Contributions to Mineralogy and Petrology*, 111(3), 329–344.
- Schaltegger, U., & Corfu, F. (1995). Late Variscan “Basin and Range” magmatism and tectonics in the Central Alps: Evidence from U–Pb geochronology. *Geodinamica Acta*, 8(2), 82–98.
- Schaltegger, U., Gnoss, E., Küpfer, Th., & Labhart, T. (1991). Geochemistry and tectonic significance of Late Hercynian potassic and ultrapotassic magmatism in the Aar Massif (Central Alps). *Schweizerische Mineralogische Und Petrographische Mitteilungen*, 71, 391–403.
- Schaltegger, U., Nowak, A., Ulianov, A., Fisher, C. M., Gerdes, A., Spikings, R., Whitehouse, M., Bindeman, I. N., Brack, P., Hanchar, J., Duff, J., Vervoort, J. D., Sheldrake, T., Caricchi, L., & Müntener, O. (2019). Zircon petrochronology and 40Ar–39Ar thermochronology of the Adamello intrusive suite, N-Italy: Monitoring the growth and decay of an incrementally assembled magmatic system. *Journal of Petrology*, 60, 701–722. <https://doi.org/10.1093/petrology/egz010>
- Schaltegger, U., Ovtcharova, M., Gaynor, S. P., Davies, J. H. F. L., Wotzlaw, J. F., Greber, N., Farina, F., Szymanowski, D., & Chelle-Michou, C. (2021). Long-term repeatability and interlaboratory reproducibility of high-precision ID-TIMS U–Pb geochronology. *Journal of Analytical and Atomic Spectrometry*, 36, 1466–1477. <https://doi.org/10.1039/D1JA00116G>
- Schoene, B., Schaltegger, U., Brack, P., Latkoczy, C., Stracke, A., Günther, D., & Samperton, K. (2012). Rates of magma differentiation and emplacement in a ballooning pluton recorded by U–Pb TIMS-TEA, Adamello batholith, Italy. *Earth and Planetary Science Letters*, 355–356, 162–173. <https://doi.org/10.1016/j.epsl.2012.08.019>
- Schulmann, K., Lexa, O., Janoušek, V., Lardeaux, J. M., & Edel, J. B. (2014). Anatomy of a diffuse cryptic suture zone: An example from the Bohemian Massif, European Variscides. *Geology*, 42(4), 275–278. <https://doi.org/10.1130/G35290.1>
- Seemann, U. (1975). Mineralogisch-petrographische und geochemische Untersuchungen der granitischen Gesteine der Val Punteglias. *Schweizerische Mineralogisch-Petrographische Mitteilungen*, 55, 257–306.
- Sergeev, S. A., Meier, M., & Steiger, R. H. (1995). Improving the resolution of single-grain U/Pb dating by use of zircon extracted from feldspar: Application to the Variscan magmatic cycle in the central Alps. *Earth and Planetary Science Letters*, 134, 37–51.
- Sláma, J., Kosler, J., Condon, D. J., Crowley, J. L., Gerdes, A., Hanchar, J. M., Horstwood, M. S. A., Morris, G. A., Nasdala, L., Norberg, N., Schaltegger, U., Schoene, B., Tubrett, M. N., & Whitehouse, M. J. (2008). Plešovice zircon—a new natural reference material for U–Pb and Hf isotopic microanalysis. *Chemical Geology*, 249(1–2), 1–35.
- Söderlund, U., Patchett, P., Vervoort, J., & Isachsen, C. (2004). The ^{176}Lu decay constant determined by Lu–Hf and U–Pb isotope systematics of Precambrian mafic intrusions. *Earth and Planetary Science Letters*, 219(3–4), 311–324.
- Tabaud, A. S., Janoušek, V., Skrzypek, E., Schulmann, K., Rossi, P., Whitechurch, H., et al. (2015). Chronology, petrogenesis and heat sources for successive Carboniferous magmatic events in the Southern-Central Variscan Vosges Mts (NE France). *Journal of the Geological Society London*, 172(1), 87–102.
- Thirlwall, M., & Anczkiewicz, R. (2004). Multidynamic isotope ratio analysis using MC–ICP–MS and the causes of secular drift in Hf, Nd and Pb isotope ratios. *International Journal of Mass Spectrometry*, 235(1), 59–81.
- Ulianov, A., Müntener, O., Schaltegger, U., & Bussy, F. (2012). The data treatment dependent variability of U–Pb zircon ages obtained using mono-collector, sector field, laser ablation ICP–MS. *Journal of Analytical and Atomic Spectrometry*, 27, 663–676. <https://doi.org/10.1039/c2ja10358c>
- Vanderhaeghe, O., Laurent, O., Gardien, V., Moyen, J. F., Gébelins, A., Chelle-Michou, C., Couzinié, S., Villaros, A., & Bellanger, M. (2020). Flow of partially molten crust controlling construction, growth and collapse of the Variscan orogenic belt: The geologic record of the French Massif Central. *Bulletin De La Société Géologique De France, BSGF*, 191, 25.
- Vermeesch, P. (2018). IsoplotR: A free and open toolbox for geochronology. *Geoscience Frontiers*, 9, 1479–1493.
- Wendt, I., & Carl, C. (1991). The statistical distribution of the mean squared weighted deviation. *Chemical Geology: Isotope Geoscience Section*, 86(4), 275–285.
- Widmann, P., Davies, J. H. F. L., & Schaltegger, U. (2019). Calibrating chemical abrasion: Its effects on zircon crystal structure, chemical composition and U–Pb age. *Chemical Geology*, 511, 1–10.
- Woodhead, J. D., & Hergt, J. M. (2005). A preliminary appraisal of seven natural zircon reference materials for in situ Hf isotope determination. *Geostandards and Geoanalytical Research*, 29, 183–195.

Publisher's Note

Springer Nature remains neutral with regard to jurisdictional claims in published maps and institutional affiliations.

Submit your manuscript to a SpringerOpen[®] journal and benefit from:

- Convenient online submission
- Rigorous peer review
- Open access: articles freely available online
- High visibility within the field
- Retaining the copyright to your article

Submit your next manuscript at ► [springeropen.com](https://www.springeropen.com)